# Relative Orientation of Peptide Planes in Proteins Is Reflected in Carbonyl−Carbonyl Chemical Shift Anisotropy Cross-Correlated Spin Relaxation

**Nikolai R. Skrynnikov,[†] Robert Konrat,[‡] D. R. Muhandiram,[†] and Lewis E. Kay*,[†]**

*Contribution from the Protein Engineering Network Centers of Excellence and Departments of Medical Genetics, Biochemistry and Chemistry, University of Toronto, Toronto, Ontario, Canada, M5S 1A8, and The Institute of Organic Chemistry, University of Innsbruck, Innrain 52, A-6020 Innsbruck, Austria*

*Received January 3, 2000. Revised Manuscript Received May 12, 2000*

**Abstract:** Experiments for measuring chemical shift anisotropy (CSA) cross-correlated spin relaxation between pairs of carbonyl spins in $^{15}N$,$^{13}C$-labeled proteins based on differences in relaxation rates of double- and zero-quantum carbonyl coherences are presented. In the case where the carbonyl spins reside on successive residues, information about the intervening ($\phi$,$\psi$) backbone dihedral angles is obtained. A good correlation between predicted and measured cross-correlation rates is observed in experiments recorded on an SH3 domain from spectrin. Cross-correlated spin relaxation between carbonyl spins residing on two peptide planes linked via hydrogen bonding can also be measured for small proteins in concentrated samples, providing information about the relative orientation of these planes, as demonstrated for the spectrin SH3 domain.

Structure determination by solution NMR spectroscopy is predicated to a large extent on the establishment of internuclear distances from the nuclear Overhauser effect and on the measurement of dihedral angles based on recording scalar couplings between NMR active spins.[2] To date, structures of a large number of proteins with molecular weights up to approximately 25 kDa have been determined using these types of restraints. More recently a number of methods have been developed allowing structural information to be obtained through measurement of so-called "projection restraints". In one set of experiments spin relaxation is used to measure the projection of one bond vector onto another or the orientation of a bond vector in a defined molecular frame.[3] Examples of protein applications include measurement of the angle between the $^1H^{\alpha}$–$^{13}C^{\alpha}$ and $^1H^N$–$^{15}N$ bond vectors of successive residues, $i-1$ and $i$, through recording double- and zero-quantum $^{13}C^{\alpha}(i-1)-^{15}N(i)$ coherences,[3−5] or determining the orientation of the $^1H^{\alpha}$–$^{13}C^{\alpha}$ vector relative to the principal axes of the $^{13}CO$ chemical shift tensor from measurement of $^{13}C^{\alpha}-^{13}CO$ double- and zero-quantum relaxation rates.[6,7] Both of these approaches provide information about the dihedral angle $\psi$. In a second class of experiments the molecule of interest is dissolved in a dilute liquid crystal solution resulting in weak alignment with the external magnetic field.[8,9] Interactions which would normally average to zero in isotropic solvent no longer do, allowing, for example, the measurement of a large number of dipolar couplings.[10,11] These couplings can be interpreted in terms of the orientation of the individual internuclear vectors in a defined molecular frame,[8] providing projection information that is similar to that obtained from the spin relaxation experiments mentioned above.

In addition to measuring dipole−dipole cross-correlated spin relaxation, which provides the relative orientation of the two dipole vectors, or dipole−chemical shift anisotropy (CSA) cross-correlation which is sensitive to the orientation of the dipole vector in the principal frame of the CSA tensor, it is also possible to measure cross-correlated spin relaxation between two CSA interactions. Assuming that the orientation of the CSA tensors and the values of their principal components are known, such measurements can provide useful structural information since they are sensitive to the projection of one CSA frame onto another. Although it has been known for some time from theoretical analyses that the difference between the double- and zero-quantum relaxation rates of a pair of spins can provide a direct measure of the cross-correlation between the CSA interactions of the two nuclei,[12,13] experimental observations of this effect have only recently appeared.[14−16] To date studies have

[†] University of Toronto.
[‡] University of Innsbruck.

(1) Wüthrich, K. *NMR of Proteins and Nucleic Acids*; John Wiley & Sons: New York, 1986.
(2) Bax, A.; Vuister, G. W.; Grzesiek, S.; Delaglio, F.; Wang, A. C.; Tschudin, R.; Zhu, G. *Methods Enzymol.* **1994**, *239*, 79−105.
(3) Reif, B.; Hennig, M.; Griesinger, C. *Science* **1997**, *276*, 1230−1233.
(4) Yang, D.; Kay, L. E. *J. Am. Chem. Soc.* **1998**, *120*, 9880−9887.
(5) Chiarparin, E.; Pelupessy, P.; Ghose, R.; Bodenhausen, G. *J. Am. Chem. Soc.* **1999**, *121*, 6876−6883.
(6) Yang, D.; Konrat, R.; Kay, L. E. *J. Am. Chem. Soc.* **1997**, *119*, 11938−11940.
(7) Yang, D.; Gardner, K. H.; Kay, L. E. *J. Biomol. NMR* **1998**, *11*, 213−220.
(8) Tjandra, N.; Bax, A. *Science* **1997**, *278*, 1111−1114.
(9) Prestegard, J. H. *Nat. Struct. Biol. NMR supplement* **1998**, *5*, 517−522.
(10) Wang, Y. X.; Marquardt, J. L.; Wingfield, P.; Stahl, S. J.; Lee-Huang, S.; Torchia, D. A.; Bax, A. *J. Am. Chem. Soc.* **1998**, *120*, 7385−7386.
(11) Yang, D.; Venters, R. A.; Mueller, G. A.; Choy, W. Y.; Kay, L. E. *J. Biomol. NMR* **1999**, *14*, 333−343.
(12) Werbelow, L. G. *J. Magn. Reson.* **1987**, *71*, 151−153.
(13) Konrat, R.; Sterk, H. *Chem. Phys. Lett.* **1993**, *203*, 75−80.
(14) Norwood, T. J.; Tillett, M. L.; Lian, L. Y. *Chem. Phys. Lett.* **1999**, *300*, 429−434.
(15) Pellecchia, M.; Pang, Y.; Wang, L.; Kurochkin, A. V.; Kumar, A.; Zuiderweg, E. R. P. *J. Am. Chem. Soc.* **1999**, *121*, 9165−9170.
(16) Pervushin, K. V.; Wider, G.; Riek, R.; Wüthrich, K. *Proc. Natl. Acad. Sci. U.S.A.* **1999**, *96*, 9607−9612.

10.1021/ja0000201 CCC: $19.00 
Published on Web 07/08/2000

not focused on using CSA−CSA cross-correlated spin relaxation as a probe of protein structure.

Herein an experiment which measures the $^{13}CO-^{13}CO$ cross-correlation rate between carbonyl carbons of successive residues in proteins is described. Because this rate is sensitive to the relative orientation of the CSA frames of the carbonyl spins, which in turn is directly related to the intervening $(\phi,\psi)$ dihedral angles, useful structural information can be obtained. This is demonstrated through an application on an $^{15}N,^{13}C,^{2}H$-labeled sample of the spectrin SH3 domain, where a good correlation between measured rates and those predicted on the basis of the high-resolution X-ray structure of the protein[17] is obtained. In addition, we demonstrate using the spectrin SH3 domain sample that, sensitivity permitting, it is possible to derive long range projection restraints by measuring $^{13}CO-^{13}CO$ cross-correlated spin relaxation involving carbonyl spins from peptide planes that are linked via hydrogen bonding.

## Materials and Methods

All spectra were recorded on an $^{15}N,^{13}C,^{2}H$-labeled sample of spectrin SH3 prepared in a manner similar to that described by Blanco et al.[18] The sample was a gift from Drs. Tanja Kortemme and Luis Serrano (EMBL). Sample conditions were 6 mM, pH 3.5, 90% $H_2O$, 10% $D_2O$, 1 $\mu$M leupeptin, 1 $\mu$M pepstatin, 800 $\mu$M Pefabloc, 100 $\mu$M DSS, 25 °C. All spectra were recorded on either Varian Inova 500 or Inova 600 MHz spectrometers. Although a concentrated sample was necessary for measuring $^{13}CO-^{13}CO$ cross-correlated spin relaxation involving carbonyl spins from peptide planes that are linked via hydrogen bonding (scheme of Figure 1b, see below), a significantly more dilute sample could be used in measuring cross-correlation between $^{13}CO$ carbons from successive residues (scheme of Figure 1a) since average S/N values of 300 (zero-quantum data) and 400 (double-quantum data) were obtained from data sets recorded at 600 MHz (see Supporting Information). Indeed, we are currently in the process of applying this methodology to maltose binding protein (42 kDa, 1.4 mM sample), and the sensitivity appears to be sufficient to extract accurate relaxation rates in this case.

For the sequence of Figure 1a data matrixes of 70 × 30* × 512* (500 MHz) or 68 × 36* × 576* (600 MHz) points were acquired in $t_1,t_2,t_3$ (where * refers to complex points), and $(t_1,t_2,t_3)$ acquisition times at 500 and 600 MHz of (60 ms, 27.6 ms, 64 ms) and (48.6 ms, 27.8 ms, 64 ms), respectively, were employed. Data sets with $\phi 3 = y,x$ were recorded in an interleaved manner and either subtracted or added to yield spectra with cross-peaks derived from double- or zero-quantum correlations, respectively, as described below. Constant-time periods, $2T_C$, of 72 and 50 ms were employed at 500 and 600 MHz, respectively. Eight transients were recorded per FID with a recycle delay of 1.6 s, resulting in net acquisition times of 30 (500 MHz) and 35 h (600 MHz). The data sets were processed using Gaussian apodization functions in $t_1$ and the $t_2$ time domain extended by mirror image linear prediction.[19] Final processed data sets were comprised of (256, 128, 1024) real data points (500 MHz) or (256, 128, 2048) real points (600 MHz) before discarding spectral regions where peaks are not found. Processing was carried out using the NMRPipe/NMRDraw suite of programs[20] and analysis performed using CAPP and PIPP.[21] A data matrix comprising 56 × 32* × 512* points corresponding to $(t_1,t_2,t_3)$ acquisition times of (47.8 ms, 29.5 ms, 64 ms) was recorded (500 MHz) using the sequence of Figure 1b with a $T_C$ value of 32.5 ms. Processing and analysis were performed in a manner identical to what is described above for the experiments of Figure 1a. A final data matrix consisting of (256, 128, 1024) real points was analyzed.

$^{15}N$ spin relaxation experiments were recorded on the $^{15}N,^{13}C,^{2}H$-labeled spectrin SH3 sample using the sequences described by Farrow et al.[22] A value of $D_{iso} = (D_{||} + 2D_{\perp}) / 3 = 0.260 \times 10^8\ s^{-1}$ ($\tau_R = 6.4$ ns) was obtained from an analysis based on $T_1/T_2$ ratios,[23−25] with $D_{||}/D_{\perp} = 1.22$, where $D_{\perp}$ and $D_{||}$ are the $x$ (or $y$) and $z$ components, respectively, of the assumed axially symmetric reorientational diffusion tensor.

The effect of relaxation coupling between various DQ/ZQ modes was investigated using complete 4 × 4 relaxation matrixes in the operator bases $C_+\tilde{C}_{\pm}$, $C_+\tilde{C}_{\pm}C_z^{\alpha}$, $C_+\tilde{C}_{\pm}N_z$, and $C_+\tilde{C}_{\pm}C_z^{\alpha}N_z$, where $C = {}^{13}CO(i)$ and $\tilde{C} = {}^{13}CO(i-1)$. All dipolar and CSA contributions in the five-spin system comprising $^{13}CO(i-1)$, $^{15}N(i)$, $^{1}H^{N}(i)$, $^{13}C^{\alpha}(i)$, and $^{13}CO(i)$ were taken into account in calculating the relaxation matrix elements. The evolution of the ZQ and DQ coherences during constant-time period $2T_C$ (Figure 1a) was computed using these relaxation matrixes. The resulting multiexponential decay curves were used to simulate $F_1$ line shapes for DQ and ZQ peaks, allowing evaluation of the peak intensities, $I_{DQ}$ and $I_{ZQ}$, from which $R_{DQ} - R_{ZQ}$ is estimated (see eq 6).

Density functional theory (DFT) computations of $^{13}CO$ CSA tensors were performed using the program deMon[26] as described in detail by Scheurer et al.[27] Molecular fragments used for CSA computations included nearby aromatic rings and electric charges on the surrounding charged amino acids. Hydrogen bonds formed by the carbonyl group of interest, CO, and the adjacent amide group, NH, were also taken into account.[27] A table (S2) of $^{13}CO$ CSA tensors computed for five pairs of hydrogen-bonded peptide planes is given in Supporting Information.

## Results and Discussion

**Description of the Experiments.** Figure 1 illustrates the pulse schemes that have been developed to measure the $^{13}CO$ CSA−CSA cross-correlated spin relaxation rate between (a) pairs of carbonyl spins that are adjacent in primary sequence and (b) between pairs of remote carbonyl spins in residues $i-1$ and $j$, that lie in peptide planes that are connected by a hydrogen bond formed by the NH of residue $i$ and the CO of $j$. The flow of magnetization is illustrated in the upper left-hand corners of each of the sequences. A description of scheme (a) is best accomplished by considering only the operators describing the important coherences at various stages in the sequence and by ignoring the factors describing the efficiency of each transfer step. Magnetization that originates on the $^{1}H^{N}$ spin of residue $i$ is transferred to the directly coupled $^{15}N$ spin and the $^{15}N$ magnetization evolves due to either the one- or the two-bond $^{15}N-^{13}C^{\alpha}$ coupling in addition to the one-bond $^{15}N-^{13}CO$ scalar coupling. Note that coherences that are generated from evolution due to all three couplings ($^{1}J_{NC\alpha}$, $^{2}J_{NC\alpha}$, and $^{1}J_{NCO}$) are selected against in the present scheme. Focusing for the moment on evolution under $^{1}J_{NC\alpha}$ and $^{1}J_{NCO}$ one obtains a term of the form $CO_z(i-1)N_z(i)C^{\alpha}_z(i)$ at point **a** in the scheme, where subscripts $x,y,z$ identify the component of spin magnetization and indices $i,i-1$ indicate the residue. Between points **a** and **b** in the sequence transverse $^{13}C^{\alpha}(i)$ magnetization evolves as a result of the $^{1}J_{C\alpha CO}$ coupling so that at point **b** the relevant operator

(17) Musacchio, A.; Noble, M.; Pauptit, R.; Wierenga, R.; Saraste, M. *Nature* **1992**, *359*, 851−855.
(18) Blanco, F. J.; Ortiz, A. R.; Serrano, L. *J. Biomol. NMR* **1997**, *9*, 347−357.
(19) Zhu, G.; Bax, A. *J. Magn. Reson.* **1990**, *90*, 405−410.
(20) Delaglio, F.; Grzesiek, S.; Vuister, G. W.; Zhu, G.; Pfeifer, J.; Bax, A. *J. Biomol. NMR* **1995**, *6*, 277−293.
(21) Garrett, D. S.; Powers, R.; Gronenborn, A. M.; Clore, G. M. *J. Magn. Reson.* **1991**, *95*, 214−220.
(22) Farrow, N. A.; Muhandiram, R.; Singer, A. U.; Pascal, S. M.; Kay, C. M.; Gish, G.; Shoelson, S. E.; Pawson, T.; Forman-Kay, J. D.; Kay, L. E. *Biochemistry* **1994**, *33*, 5984−6003.
(23) Brüschweiler, R.; Liao, X.; Wright, P. E. *Science* **1995**, *268*, 886−889.
(24) Lee, L. K.; Rance, M.; Chazin, W. J.; Palmer, A. G. *J. Biomol. NMR* **1997**, *9*, 287−298.
(25) Tjandra, N.; Feller, S. E.; Pastor, R. W.; Bax, A. *J. Am. Chem. Soc.* **1995**, *117*, 12562−12566.
(26) Malkin, V. G.; Malkina, O. L.; Eriksson, L. A.; Salahub, D. R. *Modern Density Functional Theory: A Tool for Chemistry*; Seminario, J. M. and Politzer, P., Ed.; Elsevier: Amsterdam, 1995; Vol. 2.
(27) Scheurer, C.; Skrynnikov, N. R.; Lienin, S. F.; Straus, S. K.; Brüschweiler, R.; Ernst, R. R. *J. Am. Chem. Soc.* **1999**, *121*, 4242−4251.

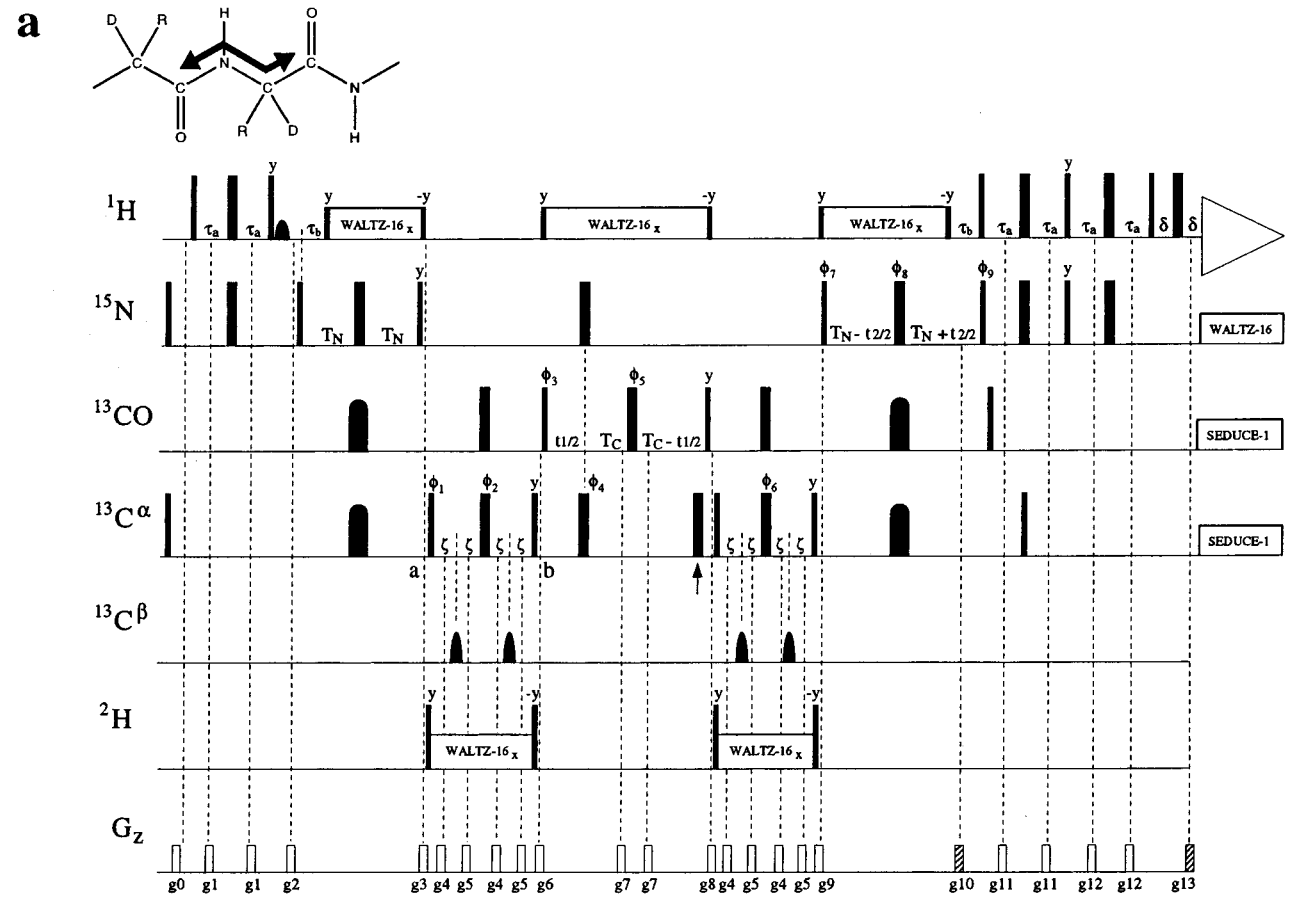


**Figure 1.** Pulse schemes to measure (a) cross-correlated spin relaxation between pairs of $^{13}$CO spins that are sequential in primary sequence and (b) between pairs of remote $^{13}$CO spins in residues $i - 1$ and $j$ with a hydrogen bond between the NH of residue $i$ and the CO of $j$ (see text). All narrow (wide) pulses are applied with flip angles of 90° (180°) and are along the $x$ axis, unless indicated otherwise. The $^1$H, $^{15}$N, and $^2$H carriers are positioned at water, 119 and 4.7 ppm, respectively. Field strengths of 36 kHz, 6.25 kHz, and 2 kHz are employed for $^1$H, $^{15}$N, and $^2$H pulses, respectively, with the exception of the shaped water selective 90° pulse (2 ms), the $^1$H WALTZ-16$_x$ decoupling elements,[62] and flanking pulses which employ a 6 kHz field and the $^2$H WALTZ-16$_x$ elements which use an 800 Hz field. **Sequence (a).** The $^{13}$C carrier is at 55 ppm until immediately prior to the $^{13}$CO pulse of phase $\phi3$ when it is moved to 176 ppm. The carrier is returned to 55 ppm after the $^{13}$CO 90° pulse of phase y. All $^{13}$C rectangular 90° (180°) pulses are applied with a field strength of $\Delta/\sqrt{15}$ ($\Delta/\sqrt{3}$) where $\Delta$ is the difference in Hz between the centers of the $^{13}$CO and $^{13}$C$^\alpha$ regions of the carbon spectrum.[63] Off-resonance pulses are applied using phase modulation of the carrier.[64,65] The simultaneous $^{13}$CO/$^{13}$C$^\alpha$ shaped pulses during the intervals of duration $2T_N$ denote adiabatic frequency-swept WURST pulses[66,67] (one for each $2T_N$ period, 80 kHz sweep, 15 kHz rf field at peak height, 300 $\mu$s duration) that invert both $^{13}$CO and $^{13}$C$^\alpha$ spins. The midpoint of each pulse is centered between the $^{13}$CO and $^{13}$C$^\alpha$ chemical shifts. The $^{13}$C$^\beta$ pulses are applied with the IBURP-2 profile,[28] are centered at 30 ppm, and have durations of 1.8 ms $\times$ (500/$\nu_o$), where $\nu_o$ is the $^1$H spectrometer frequency in MHz. Simultaneous $^{13}$CO/$^{13}$C$^\alpha$ decoupling can be used during acquisition to enhance the sensitivity for applications involving small proteins.[68] In this case, WALTZ-16 decoupling is employed where each element has the SEDUCE-1 shape[69] (325 $\mu$s). The carrier is positioned midway between the $^{13}$CO and $^{13}$C$^\alpha$ spins and the decoupling element is cosine modulated so that both types of spins are perturbed.[70] $^{15}$N decoupling during acquisition employs a 1 kHz WALTZ-16 field. The delays employed are: $\tau_a = 2.3$ ms, $\tau_b = 5.3$ ms, $T_N = 14.0$ ms, $\zeta = 2.25$ ms, $T_C = 36$ ms (500 MHz), 25 ms (600 MHz), $\delta = 500$ $\mu$s. Values of the delays may have to be adjusted for maximum sensitivity or to ensure that double- and zero-quantum correlations have sufficiently different intensities following the $2T_C$ constant-time period so that accurate cross-correlation rates can be extracted. Delays listed are for a protein tumbling with a correlation time of 6.4 ns. The phase cycle employed is: $\phi1$ = (x,−x); $\phi3$ = 2(y),2(−y); $\phi4$ = 4(x),4(−x); $\phi7$ = 4(y),4(−y); $\phi8$ = (x,−x); $\phi9$ = x; rec = 2(x,−x),2(−x,x). The $^{13}$CO 180° pulses in the intervals of duration $4\zeta$ are applied after the $^{13}$C$^\alpha$ pulses (phases $\phi2$ and $\phi6$). The phases of these $^{13}$C$^\alpha$ pulses must be adjusted for maximum signal. This is most easily accomplished by adjusting $\phi2$, for example, to give zero signal and then adding 45°to the obtained $\phi2$ value. The phase $\phi5$ must be adjusted so that absorptive $F_1$ line shapes (both double- and zero-quantum correlations) are obtained. We have ensured that all delays for power switching etc. in the pulse sequence code are carefully adjusted and absorptive $F_1$ line shapes of zero-quantum peaks are obtained. However, with $\phi5$ = x the double-quantum peaks can be slightly out of phase. Since the phase of the zero-quantum signal is not affected by $\phi5$, while double-quantum is, absorptive spectra can be readily obtained. Typically, we record a 2D $F_1$−$F_3$ projection and phase the double-quantum correlations to pure absorptive. The value of $\phi5$ is subsequently set to 1/4 of this phasing value. (The sign of $\phi5$ must be confirmed by recording an additional 2D spectrum). Quadrature detection in $t_2$ is obtained by the enhanced sensitivity pulsed field gradient method,[71,72] where for each value of $t_2$ separate data sets are recorded for (g10,$\phi9$) and (−g10,$\phi9$ + 180°). For each successive $t_2$ value $\phi7$ and the phase of the receiver are incremented by 180°.[73] Quadrature in $t_1$ is not employed. Separate data sets for $\phi3$ = y and $\phi3$ = x are recorded in an interleaved manner and subtracted or added to yield either double- or zero-quantum data sets. The duration and strengths of the gradients are: g0 = (0.5 ms, 8 G/cm), g1 = (0.5 ms, 5 G/cm), g2 = (1 ms, 15 G/cm), g3 = (0.75 ms, 20 G/cm), g4 = (0.15 ms, 18 G/cm), g5 = (0.15 ms, 25 G/cm), g6 = (0.8 ms, 25 G/cm), g7 = (0.25 ms, 12 G/cm), g8 = (1 ms, 18 G/cm), g9 = (0.4 ms, 10 G/cm), g10 = (1.25 ms, 30 G/cm), g11 = (0.4 ms, 2.9 G/cm), g12 = (0.3 ms, 5 G/cm), g13 = (0.125 ms, 29 G/cm). **Sequence (b).** The carbon carrier is at 176 ppm throughout the experiment, except during acquisition when it is moved to midway between the $^{13}$CO and $^{13}$C$^\alpha$ spins as described above. All $^{13}$C pulses are applied with a field strength of $\Delta/\sqrt{3}$. $^{13}$C$^\alpha$ decoupling is achieved with 121 ppm cosine-modulated SEDUCE decoupling (325 $\mu$s pulses). The two $^1$H 180° pulses applied during the $2T_C$ period are of the composite variety[74] ($90_x180_y90_x$) and serve to eliminate contributions from cross-correlated spin relaxation involving $^1$H$^N$($i$) $^{13}$CO($i$

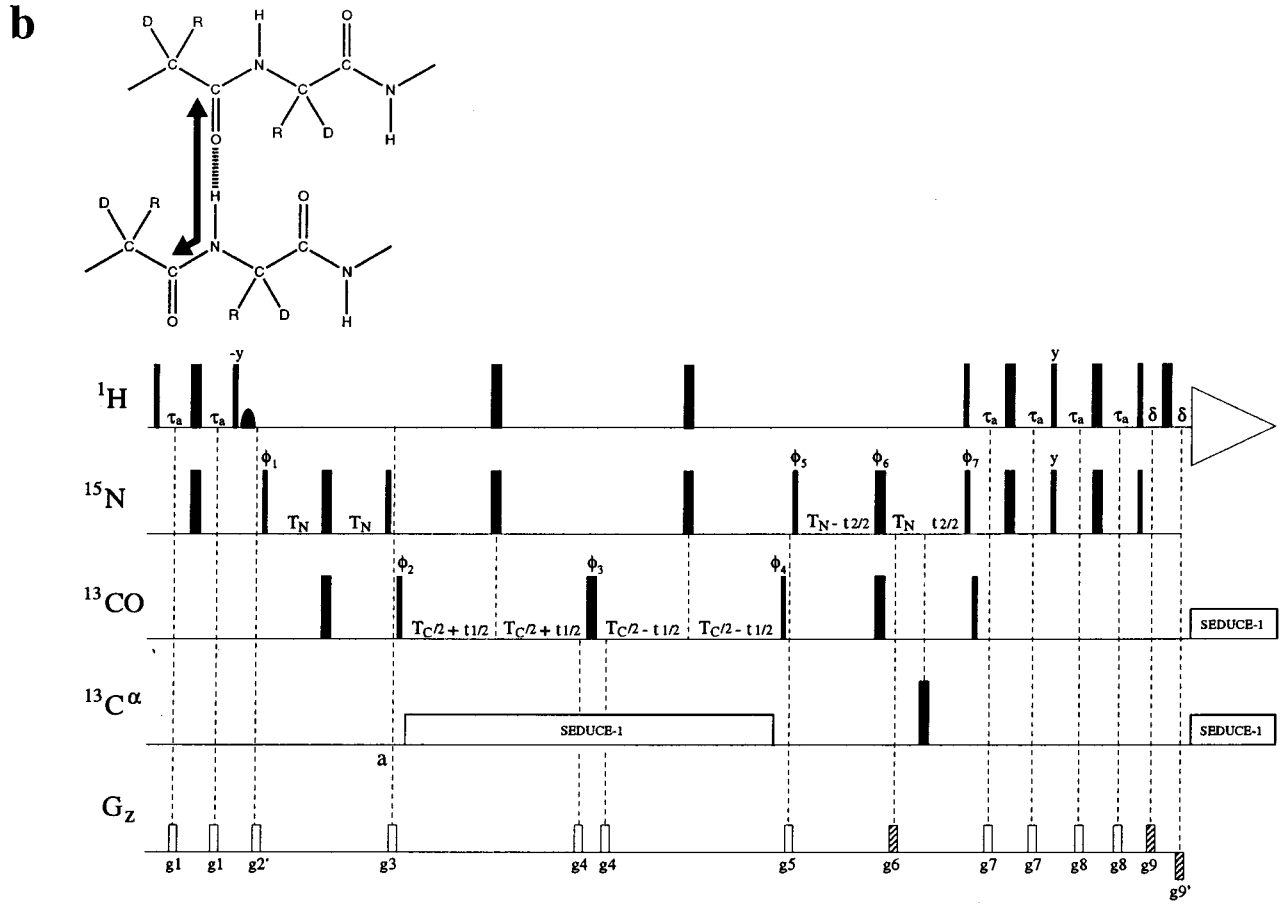


**Figure 1. (Continued)** − 1) dipolar and $^{13}$CO($j$) CSA or $^1$H$^N$($i$) $^{13}$CO($j$) dipolar and $^{13}$CO($i$ − 1) CSA interactions. The delays employed are: $\tau_a$ = 2.3 ms, $T_N$ = 81.7 ms, $T_C$ = 32.5 ms (500 MHz), $\delta$ = 250 $\mu$s. The phase cycle employed is: $\phi1$ = (x,−x); $\phi2$ = 2(y),2(−y),2(x),2(−x); $\phi5$ = 8(x), 8(−x); $\phi6$ = 2(x),2(−x); $\phi7$ = x; Rec = 4(x,−x),4(−x,x). Data sets with $\phi4$ = 4(y), 4(x) and $\phi4$ = $\phi4$ + 90° are recorded in an interleaved manner and subtracted or added to generate double- or zero-quantum data sets. The phase $\phi3$ is adjusted to ensure that correlations are pure-absorptive in the $F_1$ frequency domain, as described for the scheme of Figure 1a. Quadrature detection in $F_2$ is achieved via the enhanced sensitivity approach, while quadrature is not employed in $F_1$. The duration and strengths of the gradients are: g1 = (5 ms, 5 G/cm), g2 = (1 ms, 15 G/cm), g3 = (1 ms, 18 G/cm), g4 = (0.25 ms, 12 G/cm), g5 = (0.7ms, 20 G/cm), g6 = (1.25 ms, 30 G/cm), g7 = (0.4ms, 2.9 G/cm), g8 = (0.3 ms, 5 G/cm), g9 = (62.5 $\mu$s, 27.6 G/cm). In both sequences decoupling is interrupted during application of the gradients.[75] Pulse sequences are available upon request.

is $CO_z(i-1)N_z(i)C^\alpha{}_z(i)CO_z(i)$. The undesired evolution from $^1J_{C\alpha C\beta}$ during this period is refocused for many of the residues by application of band selective inversion pulses[28] centered at 30 ppm, resulting in significant sensitivity improvements. The $^{13}$CO 90° pulse applied immediately after point **b** ($\phi3$ = y) generates the coherence, $CO_x(i-1)N_z(i)C^\alpha{}_z(i)CO_x(i)$, which is allowed to evolve for a constant time (CT) period of duration $2T_C$. In what follows it is convenient to rewrite the operator $CO_x(i-1)N_z(i)C^\alpha{}_z(i)CO_x(i)$ as a linear combination of double- (DQ) and zero- (ZQ) quantum components according to[29]

$$\begin{aligned}&CO_x(i-1)N_z(i)C^\alpha{}_z(i)CO_x(i) = \\ &\quad 0.5N_z(i)C^\alpha{}_z(i)\{CO_x(i-1)CO_x(i) - CO_y(i-1)CO_y(i)\} + \\ &\quad 0.5N_z(i)C^\alpha{}_z(i)\{CO_x(i-1)CO_x(i) + CO_y(i-1)CO_y(i)\}\end{aligned} \quad (1)$$

where, following the notation of Sørensen et al.[29]

$$\begin{aligned}\{DQ_x\} &= \{CO_x(i-1)CO_x(i) - CO_y(i-1)CO_y(i)\} \\ \{ZQ_x\} &= \{CO_x(i-1)CO_x(i) + CO_y(i-1)CO_y(i)\} \\ \{DQ_y\} &= \{CO_x(i-1)CO_y(i) + CO_y(i-1)CO_x(i)\} \\ \{ZQ_y\} &= \{CO_y(i-1)CO_x(i) - CO_x(i-1)CO_y(i)\}\end{aligned} \quad (2)$$

Evolution of the terms in eq 1 during the CT period proceeds according to[29]

$$\begin{aligned}\{DQ_x\} &\xrightarrow{2T_C} \exp(-2R_{DQ}T_C)\,[\{DQ_x\}\cos(\omega_{CO(i-1)} + \\ &\qquad \omega_{CO(i)})t_1 + \{DQ_y\}\sin(\omega_{CO(i-1)} + \omega_{CO(i)})t_1] \\ \{ZQ_x\} &\xrightarrow{2T_C} \exp(-2R_{ZQ}T_C)[\{ZQ_x\}\cos(\omega_{CO(i-1)} - \\ &\qquad \omega_{CO(i)})t_1 + \{ZQ_y\}\sin(\omega_{CO(i-1)} - \omega_{CO(i)})t_1]\end{aligned} \quad (3)$$

where $R_{DQ}$ and $R_{ZQ}$ denote the double- and zero-quantum relaxation rates, respectively. Application of the subsequent $^{13}$CO 90° pulse gives

$$\begin{aligned}&CO_z(i-1)N_z(i)C^\alpha{}_z(i)CO_z(i)\,[\,0.5\exp(-2R_{DQ}T_C)\times \\ &\qquad \cos(\omega_{CO(i-1)} + \omega_{CO(i)})t_1 + 0.5\exp(-2R_{ZQ}T_C)\times \\ &\qquad\qquad \cos(\omega_{CO(i-1)} - \omega_{CO(i)})t_1\,]\end{aligned} \quad (4)$$

where the multiplicative factor in parentheses indicates the separate evolution pathways of double- and zero-quantum states

(28) Geen, H.; Freeman, R. *J. Magn. Reson.* **1991**, *93*, 93−141.
(29) Sørensen, O. W.; Eich, G. W.; Levitt, M. H.; Bodenhausen, G.; Ernst, R. R. *Progr. NMR Spectrosc.* **1983**, *16*, 163−192.

during $2T_C$. The spin order described in eq 4 is subsequently transferred back to observable $^1H^N$ magnetization following the reverse of the pathway outlined above. Fourier transformation of the resultant time domain data set produces a spectrum with cross-peaks at ($\omega_{CO(i-1)} \pm \omega_{CO(i)}$, $\omega_{N(i)}$, $\omega_{HN(i)}$). Note that quadrature detection in $F_1$ is not employed so that quadrature images are obtained in this dimension.

To separate double- and zero-quantum signals a second data set is recorded where the phase $\phi 3$ is incremented by 90°($\phi 3$ = x). This changes the sign of the first term of eq 1 describing the coherence at the start of the CT period and hence leads to (cf. eq 4)

$$CO_z(i-1)N_z(i)C^{\alpha}{}_z(i)CO_z(i)\,[-0.5\exp(-2R_{DQ}T_C)\times\cos(\omega_{CO(i-1)}+\omega_{CO(i)})t_1+0.5\exp(-2R_{ZQ}T_C)\times\cos(\omega_{CO(i-1)}-\omega_{CO(i)})t_1] \quad (5)$$

Addition and subtraction of data sets recorded with $\phi 3 = y,x$ thus generates two data sets with cross-peaks at ($\omega_{CO(i-1)} - \omega_{CO(i)}$, $\omega_N$, $\omega_{HN}$) (ZQ set) and ($\omega_{CO(i-1)} + \omega_{CO(i)}$, $\omega_N$, $\omega_{HN}$) (DQ set). Intensity ratios of these cross-peaks allow a direct calculation of the difference in relaxation rates between DQ and ZQ coherences, $R_{DQ} - R_{ZQ}$, via

$$R_{DQ} - R_{ZQ} = -1/(2T_C)\ln(I_{DQ}/I_{ZQ}) \quad (6)$$

where $I_{DQ}$ and $I_{ZQ}$ are the intensities of cross-peaks in the DQ and ZQ spectra.

There is an additional pathway of magnetization flow which is important to mention. The above discussion has focused on the term derived from evolution of $^{15}N$ transverse magnetization under the effect of $^1J_{NC\alpha}$ and $^1J_{NCO}$ couplings which are active during the $2T_N$ periods in the scheme of Figure 1a. However, evolution of $^{15}N$ magnetization due to both $^2J_{NC\alpha}$ and $^1J_{NCO}$ scalar couplings can also occur during $2T_N$. It is straightforward to show that this pathway results in a term of the form $C^{\alpha}{}_z(i-1)N_z(i)$ at point **b** in the scheme. Because the subsequent $^{13}CO$ pulses do not perturb $^{13}C^{\alpha}$ magnetization, this term does not evolve during $2T_C$ and is transferred back to observable $^1H^N$ magnetization by the remaining part of the sequence. Thus, correlations at the frequencies (0, $\omega_{N(i)}$, $\omega_{HN(i)}$) in ($F_1$,$F_2$,$F_3$) are observed. The intensities of these axial peaks can be quite significant, typically ranging from a similar size to several times larger than the double- or zero-quantum correlations. During data processing, axial correlations can be significantly attenuated by time domain deconvolution of the data, in an analogous fashion to the approach currently employed for minimization of the residual water signal in spectra.[30] Unfortunately the intensities of the ZQ or DQ peaks that are within 50−60 Hz of the $^{13}CO$ carrier can be affected by this procedure, and therefore these peaks cannot be used in the analysis. An alternative method that allows measurement of correlations closer to zero frequency in $F_1$ is described in the Appendix.

Figure 1b illustrates the pulse scheme that is used to measure the $^{13}CO$ cross-correlated relaxation rate involving pairs of remote $^{13}CO$ spins. The first part of the pulse scheme is similar to an HNCO,[31] where magnetization is transferred from the $^1H^N$ spin of residue $i$ to the preceding $^{13}CO$. However, the delay $2T_N$ is chosen to be considerably longer than in a standard HNCO experiment ($2.5/^1J_{NCO}$ in the present case) so that transverse $^{15}N(i)$ magnetization efficiently evolves under the effect of both $^1J_{NCO}$ and the small coupling between $^{15}N(i)$ and $^{13}CO(j)$ across the hydrogen bond,[32,33] $^{3h}J_{NCO}$ ($^{3h}J_{NCO} \approx 0.6$ Hz for residues in $\beta$-sheet regions[32]). Thus, at point **a** the operator of interest is given by $CO_z(i-1)N^{\beta}_z(i)CO_z(j)$, where $N_{z\beta}(i)$ refers to the component of $^{15}N$ magnetization coupled to the $\beta$ $^1H^N$ spin state, selected via the TROSY scheme.[34] During the subsequent CT period of duration $2T_C$ double- and zero-quantum $^{13}CO(i-1)^{13}CO(j)$ coherences are allowed to evolve in the same manner as described for the sequence of Figure 1a and the signal is subsequently returned to $^1H^N$ for observation. Two data sets with correlations at frequencies ($\omega_{CO(i-1)} + \omega_{CO(j)}$, $\omega_{N(i)} - \pi^1J_{NH}$, $\omega_{HN(i)} + \pi^1J_{NH}$) (DQ set) and ($\omega_{CO(i-1)} - \omega_{CO(j)}$, $\omega_{N(i)} - \pi^1J_{NH}$, $\omega_{HN(i)} + \pi^1J_{NH}$) (ZQ set) are obtained from which $R_{DQ} - R_{ZQ}$ is calculated according to eq 6. Axial peaks at (0, $\omega_{N(i)} - \pi^1J_{NH}$, $\omega_{HN(i)} + \pi^1J_{NH}$) are also observed in spectra recorded with the sequence of Figure 1b. As illustrated below, these peaks are significantly larger than the desired double- and zero-quantum cross-peaks since the latter are derived from magnetization transfer processes involving $^{3h}J_{NCO}$ couplings that are typically less than 1 Hz. Finally, it is worth noting that the present experiment is TROSY-based[35] while the scheme of Figure 1a is not. In most triple-resonance applications involving a small protein (a 62-residue SH3 domain was employed in the present studies) the TROSY implementation will generally be less sensitive than the corresponding non-TROSY scheme in cases where transverse $^{15}N$ magnetization evolves for delays on the order of $0.5/J_{NC\alpha}$ or $0.5/J_{NCO}$. This is the situation in experiment 1a; however, in sequence 1b the long delays employed for transfer between $^{15}N$ and $^{13}CO$ ($2.5/^1J_{NCO} \approx 163$ ms) favor the use of TROSY-based approaches.

**Multiple Quantum Spin Relaxation.** In this section, the theoretical expression for the difference in the auto-relaxation rates between double- and zero-quantum coherences comprising two $^{13}C$ spins is given. In addition, it is demonstrated that the experiments of Figure 1 directly provide, to very good approximation, the cross-correlated relaxation rates due to the interference between the two $^{13}C$ CSA interactions. In what follows we consider a spin system consisting of two $^{13}CO$ spins at adjacent sites, $\tilde{C} = {}^{13}CO(i-1)$ and $C = {}^{13}CO(i)$ and the intervening $^{15}N$, $^1H^N$, and $^{13}C^{\alpha}$ spins (see Figure 1a). To calculate contributions to relaxation from the carbonyl $^{13}C$ CSA interaction it is convenient to recast the fully asymmetric CSA tensor in terms of a sum of two axially symmetric components, so that the CSA Hamiltonian can be written in the following form:[36−39]

$$H_I = \frac{2}{3}\Delta\sigma_x\gamma_I B_0\left\{I_z D^{(2)}_{00}(\Omega_x) + \sqrt{\frac{3}{8}}\,(I_+ D^{(2)}_{0-1}(\Omega_x) - I_- D^{(2)}_{01}(\Omega_x))\right\} + \frac{2}{3}\Delta\sigma_y\gamma_I B_0\left\{I_z D^{(2)}_{00}(\Omega_y) + \sqrt{\frac{3}{8}}(I_+ D^{(2)}_{0-1}(\Omega_y) - I_- D^{(2)}_{01}(\Omega_y))\right\} \quad (7)$$

where $\Delta\sigma_x = \sigma_{xx} - \sigma_{zz}$ and $\Delta\sigma_y = \sigma_{yy} - \sigma_{zz}$, $\sigma_{xx}$, $\sigma_{yy}$, and $\sigma_{zz}$

(30) Marion, D.; Ikura, M.; Bax, A. *J. Magn. Reson.* **1989**, *84*, 425−430.
(31) Kay, L. E.; Xu, G. Y.; Yamazaki, T. *J. Magn. Reson., Ser. A* **1994**, *109*, 129−133.
(32) Cornilescu, G.; Hu, J. S.; Bax, A. *J. Am. Chem. Soc.* **1999**, *121*, 2949−2950.
(33) Cordier, F.; Grzesiek, S. *J. Am. Chem. Soc.* **1999**, *121*, 1601−1602.
(34) Yang, D.; Kay, L. E. *J. Biomol. NMR* **1999**, *13*, 3−10.
(35) Pervushin, K.; Riek, R.; Wider, G.; Wüthrich, K. *Proc. Natl. Acad. Sci. U.S.A.* **1997**, *94*, 12366−12371.
(36) Goldman, M. *J. Magn. Reson.* **1984**, *60*, 437−452.
(37) Zheng, Z.; Mayne, C. L.; Grant, D. M. *J. Magn. Reson., Ser. A* **1993**, *103*, 268−281.
(38) Bremi, T.; Brüschweiler, R. *J. Am. Chem. Soc.* **1997**, *119*, 6672−6673.
(39) Canet, D. *Concepts Magn. Reson.* **1998**, *10*, 291−297.

are the *x*, *y*, and *z* components of the CSA tensor, $\gamma_I$ is the gyromagnetic ratio of spin *I*, $B_0$ is the amplitude of the static magnetic field, $I_z$, $I_+ = I_x + iI_y$, and $I_- = I_x - iI_y$, are spin operators, $D^{(2)}_{pq}(\Omega)$ is the (*pq*) element of a second-rank Wigner matrix, and $\Omega_x$, $\Omega_y$ are two sets of Euler angles specifying the orientation of the *x*- and *y*-principal axes of the CSA tensor in the laboratory frame. Taking into account all dipolar and CSA interactions in the $\tilde{C}NH^N\,C^\alpha\,C$ spin system and using eq 7 with $I = C$, $\tilde{C}$ for $H_C$ and $H_{\tilde{C}}$, respectively, one can evaluate the auto-relaxation rate $R_{DQ}$ of the double-quantum coherence $C_+\tilde{C}_+$, as well as the auto-relaxation rate $R_{ZQ}$ of the zero-quantum coherence $C_+\tilde{C}_-$, obtaining the following expression for $R_{DQ} - R_{ZQ}$:

$$R_{DQ} - R_{ZQ} = \Gamma_{C,\tilde{C}} + \eta_{C\tilde{C},C\tilde{C}} + \sum_{M\,=\,HN,N,C_\alpha} \lambda_{CM,\tilde{C}M} \qquad (8)$$

where the first (dominant) term is the contribution from the cross-correlation between the two CSA interactions, and the other (small) terms originate from dipolar interactions:

$$\Gamma_{C,\tilde{C}} = \left(\frac{2}{3}\gamma_C B_0\right)^2 4(\Delta\sigma_x\Delta\sigma_{\tilde{x}}J_{x\tilde{x}}(0) + \Delta\sigma_y\Delta\sigma_{\tilde{y}}J_{y\tilde{y}}(0) + \Delta\sigma_x\Delta\sigma_{\tilde{y}}J_{x\tilde{y}}(0) + \Delta\sigma_y\Delta\sigma_{\tilde{x}}J_{y\tilde{x}}(0)) \qquad (9)$$

$$\lambda_{CM,\tilde{C}M} = \left(-\sqrt{6}\frac{\mu_0}{4\pi}\hbar\gamma_C\gamma_M\right)^2 \langle 1/r^3_{CM}\rangle\langle 1/r^3_{\tilde{C}M}\rangle\frac{1}{12}(8J_{CM,\tilde{C}M}(0) + 12J_{CM,\tilde{C}M}(\omega_M)) \qquad (10)$$

$$\eta_{C\tilde{C},C\tilde{C}} = \left(-\sqrt{6}\frac{\mu_0}{4\pi}\hbar\gamma_C^2\right)^2 \langle 1/r^3_{C\tilde{C}}\rangle^2\frac{1}{12}(6J_{C\tilde{C},C\tilde{C}}(2\omega_C) - J_{C\tilde{C},C\tilde{C}}(0)) \qquad (11)$$

The contribution from modulation of isotropic chemical shift by conformational exchange,[40] which can be included in eq 9, is not considered here. The spectral densities $J_{a,b}(\omega)$ in eqs 9−11 describe correlations between the pairs of axially symmetric interactions (either dipolar or CSA) denoted by vectors *a* and *b*. To evaluate these spectral densities, a motional model must be selected. The simplest model is one of isotropic overall rotation with

$$G_{a,b}(t) = \frac{1}{5}S_c{}^2 e^{-6D_{iso}t}P_2(\cos\theta_{a,b}) \qquad (12)$$

$$J_{a,b}(\omega) = \int_0^\infty G_{a,b}(t)e^{i\omega t}dt \qquad (13)$$

where $P_2(x)$ is a second-order Legendre polynomial, $\theta_{a,b}$ is the angle between the vectors *a* and *b*, $S_c$ is the order parameter describing the amplitude of motion for local fluctuations of the peptide planes,[41,42] and $D_{iso}$ is the diffusion constant for isotropic molecular tumbling. Equation 12 is valid when local motions of vectors *a* and *b* are uncorrelated or, alternatively, when the local correlation time is very short.

A more complex model of motion is one which considers anisotropic overall tumbling in addition to fast internal dynamics. Here we use the "diffusion in a cone" model developed by Lipari and Szabo[43] which is well suited for analysis of local dynamics in anisotropically tumbling molecules:

$$G_{a,b}(t) = \frac{1}{5}S_c^2\sum_{q=-2}^{2} e^{-[6D_\perp + q^2(D_{||} - D_\perp)]t}d^{(2)}_{0q}(\theta_a)d^{(2)}_{0q}(\theta_b)e^{iq(\varphi_a - \varphi_b)} \qquad (14)$$

In eq 14, $S_c$ is a fast local motion order parameter (which can be expressed as $S_c = (1/2)\cos\beta(1 + \cos\beta)$ where $\beta$ denotes the semi-angle of opening for the cone of diffusion[43]), $D_{||}$ and $D_\perp$ are the components of the anisotropic rotational diffusion tensor which is assumed to be axially symmetric, $d^{(2)}_{pq}(\theta)$ is the (*pq*) element of a reduced second-rank Wigner matrix, $\theta_a$ and $\theta_b$ are the angles that vectors *a* and *b*, respectively, make with the long axis of the diffusion tensor, and $\varphi_a - \varphi_b$ is the difference in azimuthal angles of the vectors *a* and *b* in the diffusion frame. In deriving eq 14 it was assumed that the fast local motions of vectors *a* and *b* are uncorrelated for CSA interactions of the two distinct carbonyl spins; this assumption is supported by analysis of a 1.5 ns window of a molecular dynamics trajectory of the protein ubiquitin reported by Lienin et al.[44] Note that in the case when $D_{||} - D_\perp = 0$ eqs 12 and 14 become identical.

The significance of anisotropic tumbling has been assessed by comparing calculated CSA−CSA cross-correlated relaxation rates, $\Gamma_{C,\tilde{C}}$, obtained from either eqs 9, 12, 13 (isotropic model) or, alternatively, eqs 9, 14, 13 (anisotropic model) for all pairs of adjacent residues in the spectrin SH3 domain. The parameters describing molecular tumbling have been determined from $^{15}$N relaxation data (see Materials and Methods). For both models $S_c^2 = 0.82$ was employed with CSA parameters obtained from the solid-state experiments of Teng et al.[45] on gramicidin (assuming that the orientation of the CSA axes is invariant for each peptide plane). In the case of the anisotropic model, the X-ray structure of the spectrin SH3 domain (protein database accession code 1SHG[17]) was used to establish the orientation of the vectors *a* and *b* in the diffusion frame of the molecule. The root-mean-square deviation between rates derived from the two models was small (0.51 $s^{-1}$ at 600 MHz $^1$H frequency; 0.36 $s^{-1}$ at 500 MHz). Furthermore, the use of an anisotropic model resulted in an insignificant improvement in the correlation between the calculated and experimentally measured $R_{DQ} - R_{ZQ}$ values (see Table 1). Therefore, eq 12 was chosen for further interpretation of the experimental data.

The pulse sequence shown in Figure 1a does, in fact, measure the relaxation of coherences of the form $C_+\tilde{C}_\pm C_z^a N_z$, rather than $C_+\tilde{C}_\pm$. However, the difference between double- and zero-quantum auto-relaxation rates determined in this experiment is given by an expression which is nearly identical to eqs 9−11 with the distinction that the spectral densities at the frequencies $\omega_C$ and $\omega_N$ are absent from the relaxation terms $\lambda_{CC\alpha,\tilde{C}C\alpha}$ and $\lambda_{CN,\tilde{C}N}$, respectively. Evaluating $R_{DQ} - R_{ZQ}$ in the same manner as described above, we have established that the differential relaxation measured in the experiment of Figure 1a is dominated by the CSA−CSA term, eq 9, with all other terms combined, eqs 10 and 11, responsible for a 2% contribution to $R_{DQ} - R_{ZQ}$ at 600 MHz (3% at 500 MHz).

Finally, the effects of cross-correlated cross-relaxation transfer between the coherence of interest, $C_+\tilde{C}_\pm C_z^\alpha N_z$, and other coherences over the course of the period $2T_C$ in the pulse sequence of Figure 1a has also been investigated. Although some of the transfer paths are blocked due to proton decoupling during

(40) Deverell, C.; Morgan, R. E.; Strange, J. H. *Mol. Phys.* **1970**, *18*, 553−559.
(41) Lipari, G.; Szabo, A. *J. Am. Chem. Soc.* **1982**, *104*, 4559−4570.
(42) Lipari, G.; Szabo, A. *J. Am. Chem. Soc.* **1982**, *104*, 4546−4559.
(43) Lipari, G.; Szabo, A. *J. Chem. Phys.* **1981**, *75*, 2971−2976.
(44) Lienin, S. F.; Bremi, T.; Brutscher, B.; Brüschweiler, R.; Ernst, R. R. *J. Am. Chem. Soc.* **1998**, *120*, 9870−9879.
(45) Teng, Q.; Iqbal, M.; Cross, T. A. *J. Am. Chem. Soc.* **1992**, *114*, 5312−5321.

**Table 1.** Correlation between Experimental and Calculated Values of $R_{DQ} - R_{ZQ}$[a]

| no. | no. of exptl points | structure | CSA magnitude | CSA orientation | $S_c^2$ [b] | tumbling[c] | cross-relaxn terms | terms defined by eqs 10 and 11 | slope[d] | intercept[d] | rmsd[e] |
|---|---|---|---|---|---|---|---|---|---|---|---|
| | | | | Successive Residues | | | | | | | |
| 1[f] | 96[g] | 1SHG | gramicidin[45] | gramicidin[45] | 0.82 | isotropic | − | + | $0.90 \pm 0.05$[h] | $-0.6 \pm 0.7$ | 5.37 |
| 2 | 82[i] | | | | | | | | $0.92 \pm 0.05$ | $-0.3 \pm 0.7$ | 4.78 |
| 3 | | 1AEY[j](best of 15) | | | | | | | $0.66 \pm 0.05$ | $-5.1 \pm 0.7$ | 6.71 |
| 4 | | 1AEY[j](worst of 15) | | | | | | | $0.47 \pm 0.07$ | $-5.4 \pm 1.0$ | 8.90 |
| 5 | | | cyclopeptide[45] | cyclopeptide[45] | | | | | $0.67 \pm 0.04$ | $-0.4 \pm 0.5$ | 5.76 |
| 6 | | | aminoacids[48] per-residue basis | gramicidin[45] | | | | | $0.75 \pm 0.04$ | $-0.6 \pm 0.6$ | 5.18 |
| 7 | | | tripeptide[47] | tripeptide[47] | | | | | $0.87 \pm 0.05$ | $-0.9 \pm 0.7$ | 5.53 |
| 8 | | | | | per-residue basis | | | | $0.91 \pm 0.05$ | $-0.5 \pm 0.7$ | 5.42 |
| 9 | | | | | | anisotropic | | | $0.89 \pm 0.05$ | $-0.5 \pm 0.7$ | 5.34 |
| 10 | | | | | | | +[k] | | $0.88 \pm 0.05$ | $-0.4 \pm 0.7$ | 5.38 |
| 11 | | | | | | | | − | $0.90 \pm 0.05$ | $-0.1 \pm 0.7$ | 5.38 |
| | | | | Residues Connected via Hydrogen Bond | | | | | | | |
| 12[l] | 7[m] | 1SHG | gramicidin[45] | gramicidin[45] | 0.82 | isotropic | − | + | $0.79 \pm 0.07$ | $-1.3 \pm 0.8$ | 3.54 |
| 13 | 5[n] | | | | | | | | $0.81 \pm 0.10$ | $-1.2 \pm 1.2$ | 3.61 |
| 14 | 5[n] | | DFT[o] | DFT[o] | | | | | $0.78 \pm 0.08$ | $-0.3 \pm 1.0$ | 3.29 |

[a] The cells which are left blank correspond to the same entries as in the reference rows 1 and 12. [b] Order parameters have been extracted on the basis of $^{15}N$ $T_1$, $T_2$, and $^1H-^{15}N$ NOE data using a diffusion in a cone model by Lipari and Szabo[43] including anisotropic tumbling (see text). The average order parameter determined in this manner is $S_c^2 = 0.82$. In row 8, $S_c^2 = S_c(i)S_c(i+1)$ is used on a per-residue basis, where $S_c(i)$ and $S_c(i+1)$ are the order parameters for the $^{15}N$ spins adjacent to $^{13}CO(i-1)$ and $^{13}CO(i)$, respectively. [c] Parameters of isotropic and axially symmetric anisotropic tumbling have been extracted from $^{15}N$ relaxation data using the program R2R1 by Lee et al.[24] as described in the text. [d] The slope and intercept are obtained from the linear fitting as illustrated in Figures 4 and 8. [e] rmsd $= (\sum_{k=1}^{N}((R_{DQ} - R_{ZQ})_k^{calcd} - (R_{DQ} - R_{ZQ})_k^{exptl})^2/N)^{1/2}$. [f] The correlation between the experimental and calculated $R_{DQ} - R_{ZQ}$ values is shown in Figure 4. [g] 48 cross-correlation rates measured at both 500 MHz and 600 MHz, using two repeat measurements at both fields. [h] It is interesting to note that, upon interchange of $x$ and $y$ coordinates, least-square fitting yields a slope of $0.85 \pm 0.05$ instead of the expected value $1/0.90 = 1.11$; this indicates that the value of the slope is subject to significant statistical uncertainty beyond the error bounds estimated from the linear fitting procedure. [i] 41 cross-correlation rates measured at both 500 MHz and 600 MHz. Cross-correlations for which ZQ peaks fall within 0.4 ppm of the CO carrier frequency are excluded. [j] Two structures from the cluster of 15 NMR structures (PDB accession code 1AEY[18]) which yield the lowest rmsd (best) and the highest rmsd (worst) in our analyses. [k] The calculated $R_{DQ} - R_{ZQ}$ values are obtained by including cross-relaxation between coherences $C_+\tilde{C}_\pm$, $C_+\tilde{C}_\pm C_z^\alpha$, $C_+\tilde{C}_\pm N_z$, and $C_+\tilde{C}_\pm C_z^\alpha N_z$; see Materials and Methods. [l] The correlation between the experimental and calculated values is shown in Figure 8. [m] Seven cross-correlations measured at 500 MHz, using two repeat measurements. [n] Five cross-correlations measured at 500 MHz. Two cross-correlations for which DFT computations were unsuccessful because of convergence problems are excluded. [o] Density functional theory (DFT) computations using the program deMon[26] as described in Materials and Methods.

this interval, the cross-correlated cross-relaxation between $C_+\tilde{C}_\pm C_z^\alpha N_z$ and terms of the form $C_+\tilde{C}_\pm$, $C_+\tilde{C}_\pm C_z^\alpha$, and $C_+\tilde{C}_\pm N_z$ remain active for either the entire $2T_C$ period or a portion of it ($2T_C - t_1$). Simulation of the spin evolution during the period $2T_C$ ($2T_C = 50$ ms, $^1H$ frequency 600 MHz; see Materials and Methods) established that the coupling between the coherences listed above introduces only very small changes in decay rates of double- and zero-quantum terms. For example, $R_{DQ} - R_{ZQ}$ rates computed with eqs 9−13 for all pairs of successive residues in the spectrin SH3 domain differ from rates calculated with $4 \times 4$ relaxation matrixes by 0.3 $s^{-1}$ on average (rmsd 0.4 $s^{-1}$). Moreover, inclusion of cross-relaxation does not improve the agreement between experimental and calculated rates, as shown in Table 1.

Although the calculations discussed in this section have been described in the context of the experiment of Figure 1a, a similar analysis for the experiment of Figure 1b establishes that accurate CSA−CSA cross-correlated relaxation rates are obtained in this case as well. The main distinction of the experiment presented in Figure 1b is that TROSY-type coherences, $C_+\tilde{C}_\pm N_z^\beta$, are present during the period $2T_C$ so that proton 180° pulses must be applied during this interval in order to suppress remote dipolar-CSA cross-correlations[6,46] which would otherwise contribute directly to measured $R_{DQ} - R_{ZQ}$ (see figure caption).

**Protein Applications.** Figure 2 illustrates $F_1-F_3$ cross-sections of double- and zero-quantum data sets at the $^{15}N$ chemical shifts of Thr 37 (a) and Val 44 (b). In addition 1D projections of the spectra from a data matrix comprising both double- and zero-quantum $F_1$ correlations are illustrated. Note that in the present case the axial peaks have been suppressed by time-domain deconvolution of the data, as described above. Ser 36 and Thr 37 are part of the non-Src loop connecting strands $\beta$4 and $\beta$5 and the $(\phi,\psi)$ dihedral angles of Thr 37 are (−67°, −34°). In contrast, Lys 43 and Val 44 are part of strand $\beta$5, $(\phi,\psi) = (-135°, 171°)$ for Val 44, with the carbonyl oxygens and amide protons of both residues involved in hydrogen bonding. As Figure 2 readily suggests, there are significant differences between $R_{DQ} - R_{ZQ}$ for the Ser 36/Thr 37 (−17.4 $s^{-1}$) and Lys 43/Val 44 (7.5 $s^{-1}$) pairs, illustrating the sensitivity of the measured cross-correlated relaxation rates to local geometry.

A comparison of $R_{DQ} - R_{ZQ}$ values measured at 600 and 500 MHz is illustrated in Figure 3, with excellent correlation observed between these two data sets. Because $R_{DQ} - R_{ZQ}$ rates are dominated by the $^{13}CO-^{13}CO$ CSA cross-correlation term, which scales as the square of the field (see eq 9 above), a slope of 1.44 ($600^2/500^2$) is expected for this correlation. A slope of $1.48 \pm 0.02$ is obtained from the experimental data (intercept of $0.17 \pm 0.15$). This result, based on comparison of 500 and 600 MHz data, Figure 3, provides strong support to the conclusion reached in the previous section that differences in double- and zero-quantum relaxation rates can be interpreted in terms of $^{13}CO-^{13}CO$ cross-correlation exclusively and hence can be directly related to local structure.

(46) Brutscher, B.; Skrynnikov, N. R.; Bremi, T.; Brüschweiler, R.; Ernst, R. R. *J. Magn. Reson.* **1998**, *130*, 346−351.

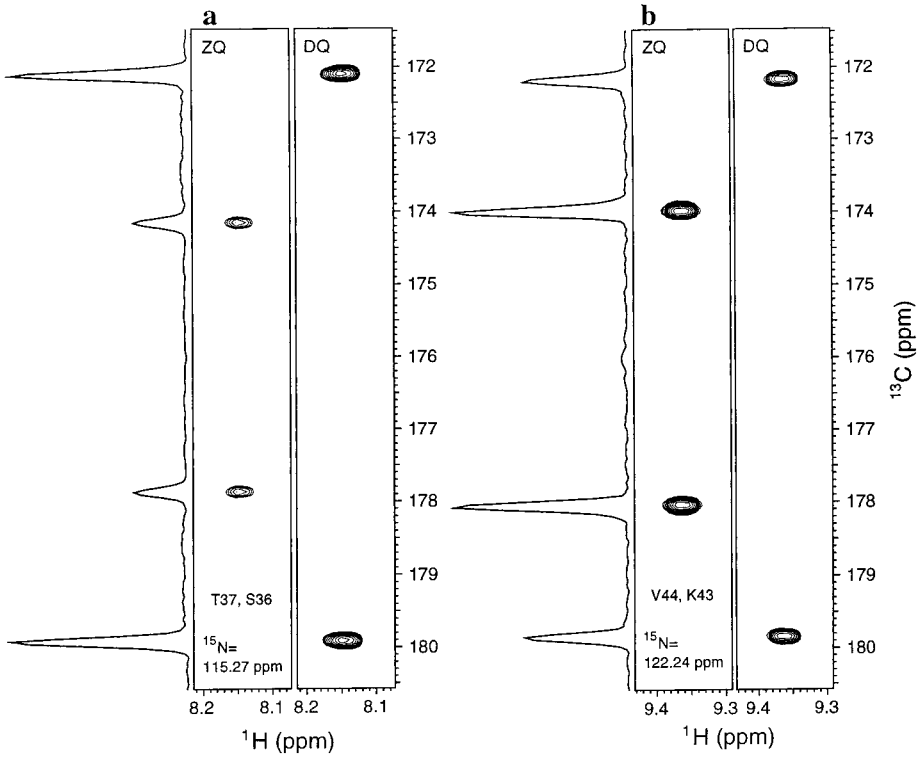


**Figure 2.** $F_1-F_3$ cross-sections of double- (DQ) and zero-quantum (ZQ) data sets recorded at 500 MHz on a sample of the spectrin SH3 domain using the sequence of Figure 1a. Slices at the $^{15}$N chemical shifts of Thr 37 (a) and Val 44 (b) showing DQ/ZQ peaks involving $^{13}$CO spins of Ser 36/Thr 37 (a) and Lys 43/Val 44 (b) are illustrated along with 1D projections of the data from a matrix containing both double- and zero-quantum $F_1$ correlations. Axial peaks have been suppressed by time-domain deconvolution of the data,[30] but could equally well be eliminated by the procedure described in the Appendix.

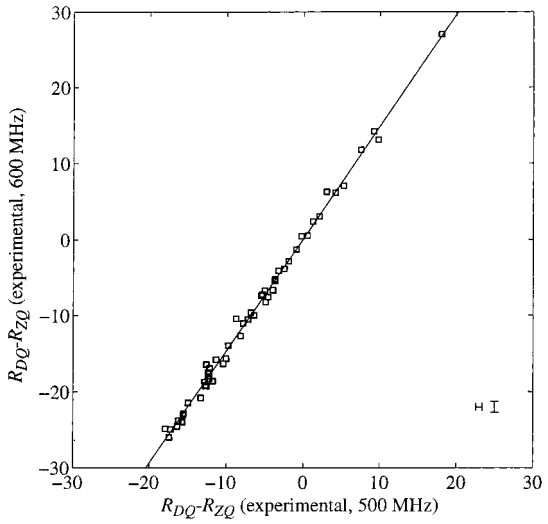


**Figure 3.** Correlation of $R_{DQ} - R_{ZQ}$ values measured at 600 and 500 MHz using the sequence of Figure 1a. Because the dominant term in the $R_{DQ} - R_{ZQ}$ rates derives from $^{13}$CO−$^{13}$CO CSA cross-correlation, eq 9, a slope of 1.44 is expected for this dependence. The best fit line for the data has a slope of 1.48 ± 0.02 and a *y*-intercept of 0.17 ± 0.15 $s^{-1}$. The experimental uncertainty for 500 and 600 MHz data is illustrated by horizontal and vertical bars in the lower right corner with the lengths of the bars equal to twice the rmsd between the repeat measurements.

To quantitate the relation to local structure we have calculated $R_{DQ} - R_{ZQ}$ rates using the 1.8 Å resolution crystal structure of the spectrin SH3 domain[17] and compared the results with the values measured at both 500 and 600 MHz. Figure 4 shows the correlation between experiment and theory, where theoretical rates have been calculated using eqs 8−13 with $^{13}$CO CSA parameters reported by Teng et al.[45] for gramicidin A [($\sigma_{xx}$, $\sigma_{yy}$, $\sigma_{zz}$) = (244, 178, 90) ppm with an angle of 8° between the carbonyl bond and the *y* axis of the CSA tensor]. A linear correlation between calculated and measured $R_{DQ} - R_{ZQ}$ values is observed with a slope of 0.90 ± 0.05 and a root-mean-square deviation (rmsd) between calculated and experimental data of 5.4 $s^{-1}$ (see first row in Table 1). It is noteworthy that if the two pairs of residues marked by daggers in Figure 4 (Glu 45/Val 46, adjacent to Asn 47 which has abnormally high B-factors, and Lys 60/Leu 61, adjacent to the C-terminus of the 62-residue domain) are removed, the rmsd decreases to 4.7 $s^{-1}$. The level of agreement between calculated and observed rates is slightly worse than what has been obtained in cross-correlation experiments on ubiquitin which are sensitive to the orientation of the $H^{\alpha}-C^{\alpha}$ bond vector in the $^{13}$CO CSA frame.[6] In the later case an rmsd between predicted and observed $^{1}H^{\alpha}-^{13}C^{\alpha}$ dipolar/$^{13}$CO CSA cross-correlation rates, $\Gamma_{H\alpha C\alpha,CO}$, of 1.6 $s^{-1}$ has been obtained for a range of $\Gamma_{H\alpha C\alpha,CO}$ values approximately 2.5 times smaller than the range of $\Gamma_{C,\tilde{C}}$ values measured in the present experiment.

The spread in experimental vs calculated values observed in Figure 4 likely reflects the fact that uniform $^{13}$CO CSA parameters have been employed, that the effects of dynamics may not be fully taken into account in our treatment (in addition, possible contributions from chemical exchange have been disregarded), and that the cross-correlation rates are very sensitive to the relative orientations of peptide planes and hence reflect subtle structural differences between the solution and crystal states of the protein (see below). Table 1 illustrates the correlation between experimental and calculated $R_{DQ} - R_{ZQ}$ values, obtained with a number of different models and input parameters. As demonstrated by rows 1 and 3, 4 in Table 1, the level of agreement between the calculated and experimental

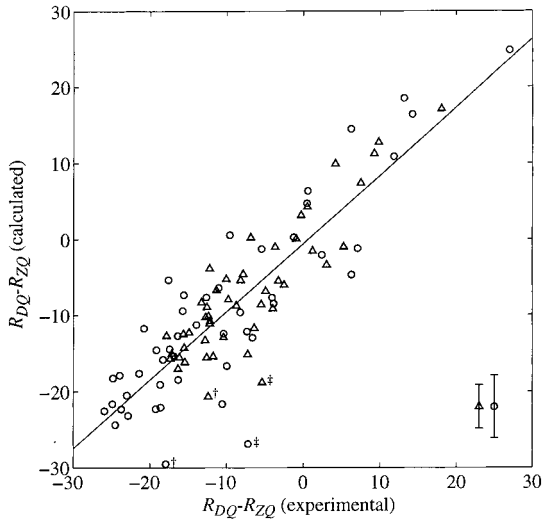


**Figure 4.** Correlation of calculated and measured (experiment of Figure 1a) $R_{DQ} - R_{ZQ}$ values (Δ: 500 MHz data; ○: 600 MHz data). Calculated rates employ CSA parameters of Teng et al.[45] for gramicidin A [$(\sigma_{xx},\sigma_{yy},\sigma_{zz})$ = (244, 178, 90) ppm with $x$ and $y$ axes of the CSA tensor in the peptide plane and the $y$ axis forming an angle of 8° with the carbonyl bond]. The best fit line has a slope of 0.90 ± 0.05 and a $y$-intercept of $-0.6 \pm 0.7 s^{-1}$ (see first row in Table 1). The vertical bars at the lower right-hand side of the figure (through the triangle and circle) indicate the typical difference (rmsd) in calculated $R_{DQ} - R_{ZQ}$ values assuming CSA parameters measured for gramicidin A or, alternatively, for a cyclopeptide in studies by Teng et al.[45] The data corresponding to the pair of residues Lys 60/Leu 61 and Glu 45/Val 46 are marked by the dagger and double dagger, respectively (see text).

values of $R_{DQ} - R_{ZQ}$ strongly depends on the quality of the structure used for the calculations. The use of low-resolution NMR structures[18] results in much higher rmsd values compared to the high-resolution X-ray structure,[17] as well as low slope values for the best-fit line. This observation underscores the sensitivity of $R_{DQ} - R_{ZQ}$ to variations in molecular structure.

Furthermore, comparison of rows 1 and 5−7 in Table 1 shows that the slope of the best-fit line can vary significantly depending on the choice of CSA parameters.[45,47,48] The dependence on CSA values is also illustrated in Figure 4 where the rmsd in $R_{DQ} - R_{ZQ}$ calculated using two different sets of CSA parameters is indicated by vertical bars. In this regard, CSA values calculated with the density functional theory program deMon[26] (see Materials and Methods) have been used for interpretation of the data obtained in the experiment of Figure 1b. The agreement between experimental and theoretical $R_{DQ} - R_{ZQ}$ values appears to be slightly improved when DFT-derived CSA parameters are used, cf. rows 13 and 14 in Table 1. DFT calculations of the carbonyl CSA values for all residues in the spectrin SH3 domain are currently in progress.

In addition, we have explored whether differences in dynamics between sites might account in part for the rmsd values observed in Table 1. In this case, $S_c^2 = S(i)S(i+1)$ has been used in evaluating eq 12 where $S(i)$ and $S(i+1)$ are the order parameters extracted from spin relaxation data for $^{15}$N spins adjacent to the carbonyls of interest. No improvement was observed (cf. row 8 in Table 1), perhaps due to the poor correlation between order parameters determined from $^{13}$CO and $^{15}$N spin relaxation.[49]

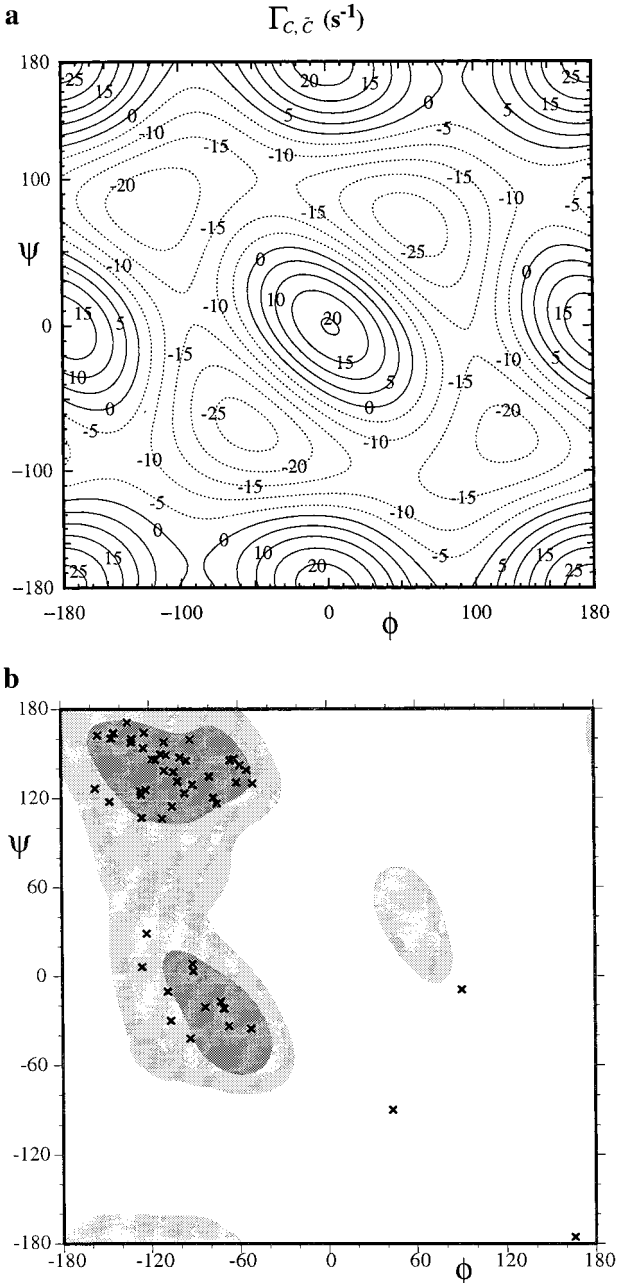


**Figure 5.** (a) Contribution to $R_{DQ} - R_{ZQ}$ from $^{13}$CO−$^{13}$CO cross-correlated spin relaxation, $\Gamma_{C,\tilde{C}}$, eq 9, at 600 MHz ($^1$H frequency) for a pair of sequential $^{13}$CO spins as a function of the intervening dihedral angles $(\phi,\psi)$ using gramicidin CSA parameters from Teng et al.[45] Allowed regions of $(\phi,\psi)$ space are shown in panel (b) with the probability of a given $(\phi,\psi)$ value indicated by shading.[76] $(\phi,\psi)$ values derived for pairs of successive residues in the X-ray structure of the spectrin SH3 domain[17] are denoted by the symbol ×.

Figure 5a illustrates the sensitivity of the $^{13}$CO−$^{13}$CO cross-correlated spin relaxation rate involving $^{13}$CO spins from adjacent peptide planes to the intervening dihedral angles $(\phi,\psi)$. The rates were predicted for a dipeptide fragment assuming CSA parameters derived by Teng et al.,[45] isotropic tumbling with a correlation time of 6.4 ns and a field of 600 MHz. The region of accessible $(\phi,\psi)$ space is illustrated in the Ramachandran plot shown in Figure 5b, with crosses denoting points obtained from the crystal structure of the spectrin SH3 domain.[17] Thus, while a measured cross-correlation rate is consistent with many $(\phi,\psi)$ values, most of the possibilities can be eliminated by

(47) Stark, R. E.; Jelinski, L. W.; Ruben, D. J.; Torchia, D. A.; Griffin, R. G. *J. Magn. Reson.* **1983**, *55*, 266−273.
(48) Ye, C.; Fu, R.; Hu, J.; Hou, L.; Ding, S. *Magn. Res. Chem.* **1993**, *31*, 699−704.
(49) Fischer, M. W. F.; Zeng, L.; Pang, Y.; Hu, W.; Majumdar, A.; Zuiderweg, E. R. P. *J. Am. Chem. Soc.* **1997**, *119*, 12629−12642.

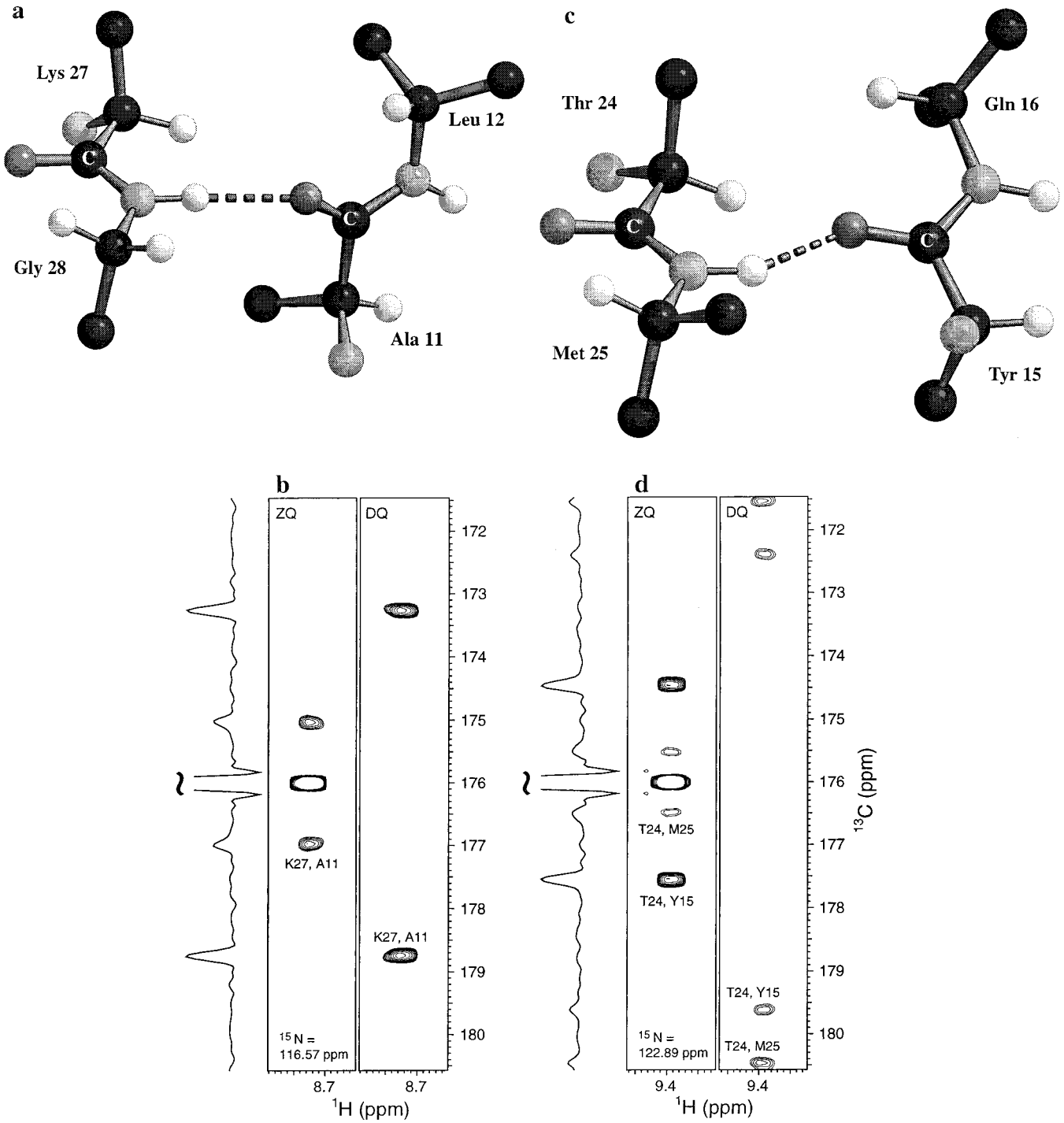


**Figure 6.** (a) Structure of the molecular fragment containing the H-bond donor/acceptor pair involving the NH of Gly 28 and the CO of Ala 11 and (b) corresponding cross-sections from DQ and ZQ quantum data sets illustrating $F_1$ coherences derived from the carbonyls of Lys 27 and Ala 11. (c) Structure of molecular fragment containing the H-bond donor/acceptor pair involving the NH of Met 25 and the carbonyl of Tyr 15 and (d) corresponding cross-sections illustrating $F_1$ DQ/ZQ correlations involving carbonyl spins of Thr 24 and Tyr 15. In (a) and (c) the dipeptide geometries are taken from the X-ray structure of the spectrin SH3 domain.[17] In (b) and (d) 1D projections from a data set containing both DQ and ZQ coherences are shown to emphasize differences in double- and zero-quantum relaxation rates.

considering only those regions in dihedral angle space that are significantly populated. Additionally, backbone chemical shift information can be used to distinguish between multiple solutions.[50,51]

As described by Reif et al.[3], projection measurements using cross-correlated spin relaxation should not necessarily be restricted to those involving interactions between intraresidue spins or spins from sequential residues. In principle, so long as coherences can be created between a pair of spins that are influenced strongly by cross-correlated interactions it may be possible to obtain projections, irrespective of the location of the spins in the molecule. Unfortunately, in most cases it is difficult to create the appropriate coherences involving remote spins since the transfer of magnetization to distal sites is generally inefficient in macromolecules. The existence of small

(50) Wishart, D. S.; Sykes, B. D. *J. Biomol. NMR* **1994**, *4*, 171−180.

(51) Cornilescu, G.; Delaglio, F.; Bax, A. *J. Biomol. NMR* **1999**, *13*, 289−302.

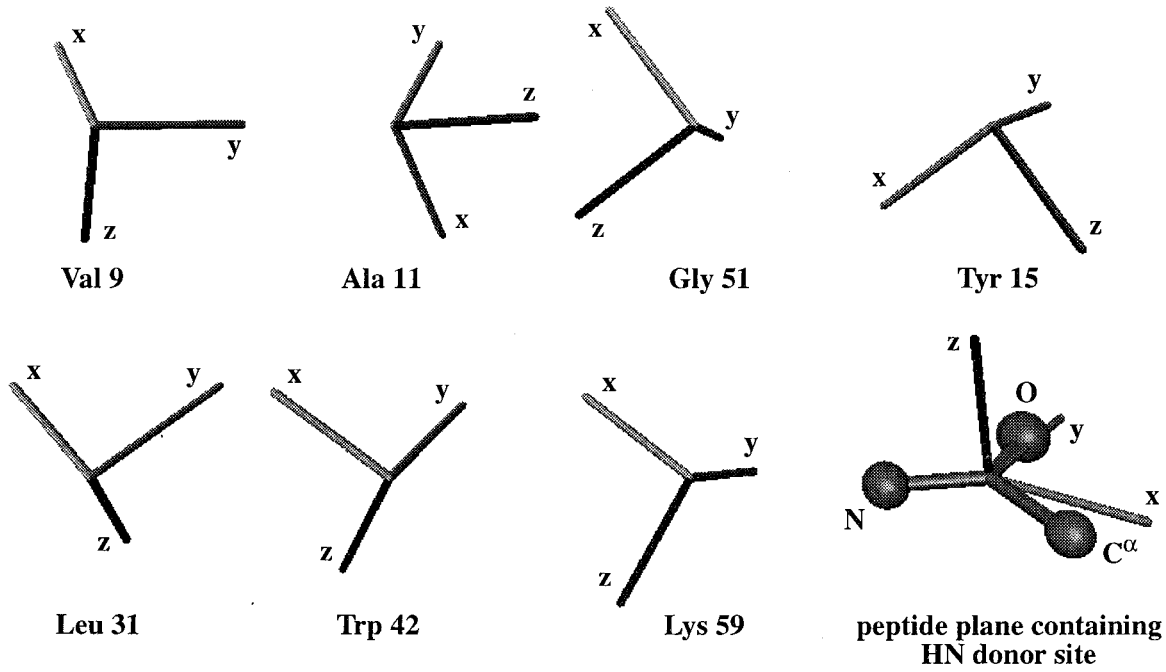


**Figure 7.** Relative orientations of the CSA tensors of the carbonyl spins for which long-range correlations in double- and zero-quantum spectra of the spectrin SH3 domain are observed. The H-bond donor peptide planes of each of the 7 donor/acceptor pairs are superimposed (lower right) and the $^{13}$CO CSA tensors for all of the acceptor carbonyl sites rotated accordingly and displayed. The orientations of the CSA tensors are derived from the X-ray structure 1SHG[17] using parameters reported by Teng et al.[45] for gramicidin A. The residue numbers for amino acids containing the acceptor carbonyl sites are indicated below each set of CSA principal axes.

but measurable remote scalar couplings between $^{15}$N and $^{13}$CO heavy atoms of H-bond donor/acceptor pairs[32,33] ($^{3h}J_{NCO} \approx 0.6$ Hz in $\beta$-sheets) suggests that it may be possible to transfer magnetization between regions of a molecule that are far removed in primary sequence. Thus, using the sequence of Figure 1b described above it is possible to create double- and zero-quantum coherences between distal carbonyl carbon spins (see the upper left-hand section of Figure 1b) and, in principle, get structural information characterizing the relative orientations of the two $^{13}$CO CSA tensors.

Figures 6a and 6c show the X-ray structures of the molecular fragments which contain the H-bond donor/acceptor pairs connecting the (a) NH of Gly 28 with the CO of Ala 11 and (c) the NH of Met 25 with the CO of Tyr 15 from the spectrin SH3 domain. Figures 6b and 6d show cross-sections from double- and zero-quantum data sets resulting from the evolution of coherences involving the two $^{13}$CO carbons marked in the plot of Figures 6a and 6c, respectively. 1D projections of the data from a data set containing both double- and zero-quantum correlations are displayed on the sides of the 2D spectra. The strong axial correlations have not been eliminated by time-domain deconvolution of the data in this case. Of note is the sign reversal in the rate $R_{DQ} - R_{ZQ}$ in these two examples, suggesting that there are important differences in structure between these two sites. The solution NMR structure of the protein[18] confirms this, as it shows that Ala 11 resides at the C-terminal end of strand $\beta$1 and Gly 28 is part of a $\beta$-bulge between $\beta$3 and $\beta$4, while Tyr 15 and Met 25 belong to antiparallel $\beta$-strands, $\beta$2 and $\beta$3, respectively. This is illustrated more clearly in Figure 7 showing the relative orientation of the CSA tensors of the carbonyl spins for which long-range correlations have been detected. In this diagram the peptide planes containing the H-bond donor sites are superimposed and the $^{13}$CO CSA tensors for all of the acceptor carbonyl sites are rotated accordingly and displayed. The relative orientations of a number of the CSA tensors are quite distinct. However, the relative orientations of the $^{13}$CO CSA tensors in Trp 42/Phe 52 and Lys 59/Val 9 pairs of residues are similar. Thus, $R_{DQ} - R_{ZQ}$ values derived from DQ/ZQ coherences established between $^{13}$CO spins for these two pairs of residues are expected to be close. Indeed, rates of $8.2 \pm 2.3 s^{-1}$ (Trp 42/Phe 52) and $12.4 \pm 1.2 s^{-1}$ (Lys 59/Val 9) have been measured.

Figure 8 illustrates the correlation between the predicted and experimental $R_{DQ} - R_{ZQ}$ rates that have been measured for remote $^{13}$CO spins. The fact that rates from only seven pairs of residues (listed in Table S2) could be quantitated and that large errors were obtained underscores the difficulties in measuring projections involving remote spins. Nevertheless, a quite acceptable level of agreement between calculated and observed rates is obtained (rmsd of 3.5 $s^{-1}$, 500 MHz). The results from the fit are summarized in the bottom three rows of Table 1, including the results obtained with DFT-derived CSA tensors.

As Figure 5a illustrates, $^{13}$CO−$^{13}$CO cross-correlated spin relaxation involving carbonyl spins on adjacent residues is sensitive to the intervening ($\phi$,$\psi$) dihedral angles. In the case of remote correlations, $R_{DQ} - R_{ZQ}$ values depend on the three Euler angles ($\alpha$,$\beta$,$\gamma$) which describe the transformation from one $^{13}$CO CSA frame to the other. Figure 9 illustrates the sensitivity of $R_{DQ} - R_{ZQ}$ to slight changes in relative orientation of peptide planes for Tyr 15 and Thr 24, Figure 6c. In these calculations the CSA frame of Thr 24 is kept fixed while the CSA frame of Tyr 15 is rotated through an angle $\omega = 5°$ about an axis oriented at polar angles ($\Theta$,$\Phi$) with respect to the original PDB coordinate system. Cross-correlation rates as a function of ($\Theta$,$\Phi$) calculated for a $^1$H frequency of 500 MHz are plotted in Figure 9. Although the exact details will vary for each pair of residues, it is quite clear from this example that the cross-correlation rates are very sensitive to the relative orientation of the CSA tensors.

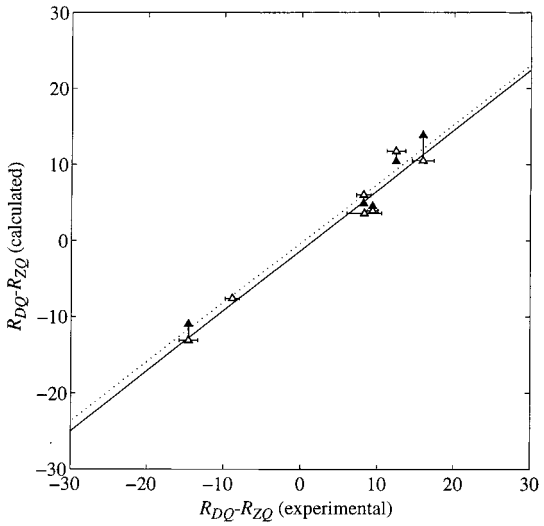


**Figure 8.** Correlation between calculated and experimental $R_{DQ} - R_{ZQ}$ rates from remote cross-correlations involving $^{13}CO$ spins connected via H-bonds in spectrin SH3. The calculated values are obtained using the gramicidin CSA parameters from Teng et al.[45] (open triangles) or, where available, CSA parameters from DFT computations (filled triangles). The horizontal bars indicate the experimental error estimated on the basis of the signal-to-noise ratio. The lines correspond to the least-squares fits between experimental rates and rates calculated using the CSA parameters from Teng et al. (solid) or DFT calculations (dotted).

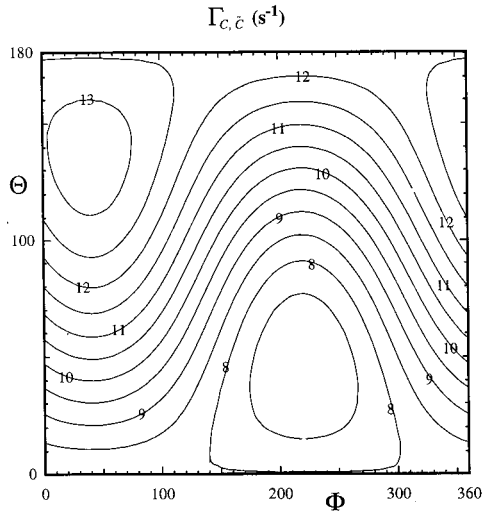


**Figure 9.** Dependence of the long-range $^{13}CO-^{13}CO$ cross-correlated spin relaxation rate $\Gamma_{C,\tilde{C}}$, eq 9, on small changes in the relative orientation of the $^{13}CO$ CSA tensors. The H-bond pair illustrated in Figure 6c was chosen to produce this plot (NH of Met 25, CO of Tyr 15 corresponding to DQ/ZQ coherences involving carbonyl spins from Thr 24 and Tyr 15). The carbonyl CSA tensor of Tyr 15 is rotated by a fixed angle of 5° about an axis with an orientation described by the polar angles (Θ,Φ) in the original X-ray coordinate system and the rate $\Gamma_{C,\tilde{C}}$ ($s^{-1}$) is computed and plotted as a function of (Θ,Φ).

## Summary

In recent years the importance of cross-correlated spin relaxation in protein NMR spectroscopy has increased dramatically. Applications to sensitivity enhancement in spectra of high molecular weight proteins via the TROSY effect[35,52,53] have been reported, measurements of cross-correlated spin relaxation rates as a probe of protein dynamics have been described,[15,46,49,54,55] and experiments for obtaining structural information through the measurement of projection restraints have appeared.[3,5,6,56−59] Recently, Sprangers et al.[60] have used cross-correlation-based structural restraints in NMR protein structure calculations by refining against an additional potential energy term added to the program CNS.[61] Although the functional dependence of the backbone dihedral angles on cross-correlated relaxation rates is multivalued (cf. Figure 5a), the ambiguities can be resolved by using a sufficient number of additional restraints in structure-refinement protocols. In the present report we have also focused on structural applications of cross-correlation and have presented two triple-resonance experiments for measuring $^{13}CO-^{13}CO$ cross-correlated spin relaxation in $^{15}N,^{13}C$-labeled proteins. In the case of correlations between sequential carbonyl spins, the measured relaxation rates are sensitive to the intervening $(\phi,\psi)$ dihedral angles, providing useful structural information. A strong correlation between rates measured in the spectrin SH3 domain and values calculated from an X-ray structure of the protein have been obtained, suggesting the possibility of using these rates in a structure refinement protocol following the approach of Sprangers et al.[60] It is also possible to generate double- and zero-quantum $^{13}CO-^{13}CO$ coherences between carbonyl spins separated by many residues in primary sequence in cases where these spins are located in peptide planes linked by hydrogen bonds. Such correlations are generally weak since they result from magnetization transfer steps with small active couplings. To the best of our knowledge this is the first time that such long-range projection restraints have been obtained from cross-correlated spin relaxation in proteins.

(52) Salzmann, M.; Pervushin, K.; Wider, G.; Senn, H.; Wüthrich, K. *Proc. Natl. Acad. Sci. U.S.A.* **1998**, *95*, 13585−13590.
(53) Yang, D.; Kay, L. E. *J. Am. Chem. Soc.* **1999**, *121*, 2571−2575.
(54) Yang, D.; Mittermaier, A.; Mok, Y. K.; Kay, L. E. *J. Mol. Biol.* **1998**, *276*, 939−954.
(55) Yang, D.; Mok, Y. K.; Muhandiram, D. R.; Forman-Kay, J. D.; Kay, L. E. *J. Am. Chem. Soc.* **1999**, *121*, 3555−3556.
(56) Carlomagno, T.; Felli, I. C.; Czech, M.; Fischer, R.; Sprinzl, M.; Griesinger, C. *J. Am. Chem. Soc.* **1999**, *121*, 1945−1948.
(57) Blommers, M. J. J.; Stark, W.; Jones, C. E.; Head, D.; Owen, C. E.; Jahnke, W. *J. Am. Chem. Soc.* **1999**, *121*, 1949−1953.
(58) Felli, I. C.; Richter, C.; Griesinger, C.; Schwalbe, H. *J. Am. Chem. Soc.* **1999**, *121*, 1956−1957.
(59) Reif, B.; Steinhagen, H.; Junker, B.; Reggelin, M.; Griesinger, C. *Angew. Chem., Int. Ed. Engl.* **1998**, *37*, 1903−1906.
(60) Sprangers, R.; Bottomley, M. J.; Linge, J. P.; Schultz, J.; Nilges, M.; Sattler, M. *J. Biomol. NMR* **2000**, *16*, 47−58.
(61) Brünger, A. T.; Adams, P. D.; Clore, G. M.; DeLano, W. L.; Gros, P.; Grosse-Kunstleve, R. W.; Jiang, J.; Kuszewski, J.; Nilges, M.; Pannu, N. S.; Read, R. J.; Rice, L. M.; Simonson, T.; Warren, G. L. *Acta Crystallogr.* **1998**, *D54*, 905−921.
(62) Shaka, A. J.; Keeler, J.; Frenkiel, T.; Freeman, R. *J. Magn. Reson.* **1983**, *52*, 335−338.
(63) Kay, L. E.; Ikura, M.; Tschudin, R.; Bax, A. *J. Magn. Reson.* **1990**, *89*, 496−514.
(64) Boyd, J.; Soffe, N. *J. Magn. Reson.* **1989**, *85*, 406−413.
(65) Patt, S. L. *J. Magn. Reson.* **1992**, *96*, 94−102.
(66) Kupce, E.; Freeman, R. *J. Magn. Reson., Ser. A.* **1995**, *115*, 273−276.
(67) Bohlen, J.-M.; Rey, M.; Bodenhausen, G. *J. Magn. Reson.* **1989**, *84*, 191−197.
(68) Yang, D.; Kay, L. E. *J. Biomol. NMR* **1999**, *14*, 273−276.
(69) McCoy, M. A.; Mueller, L. *J. Am. Chem. Soc.* **1992**, *114*, 2108−2112.
(70) McCoy, M. A.; Mueller, L. *J. Magn. Reson.* **1992**, *98*, 674−679.
(71) Kay, L. E.; Keifer, P.; Saarinen, T. *J. Am. Chem. Soc.* **1992**, *114*, 10663−10665.
(72) Schleucher, J.; Sattler, M.; Griesinger, C. *Angew. Chem., Int. Ed. Engl.* **1993**, *32*, 1489−1491.
(73) Marion, D.; Ikura, M.; Tschudin, R.; Bax, A. *J. Magn. Reson.* **1989**, *85*, 393−399.
(74) Levitt, M.; Freeman, R. *J. Magn. Reson.* **1978**, *33*, 473−476.
(75) Kay, L. E. *J. Am. Chem. Soc.* **1993**, *115*, 2055−2057.
(76) Koradi, R.; Billeter, M.; Wüthrich, K. *J. Mol. Graphics* **1996**, *14*, 51−55.

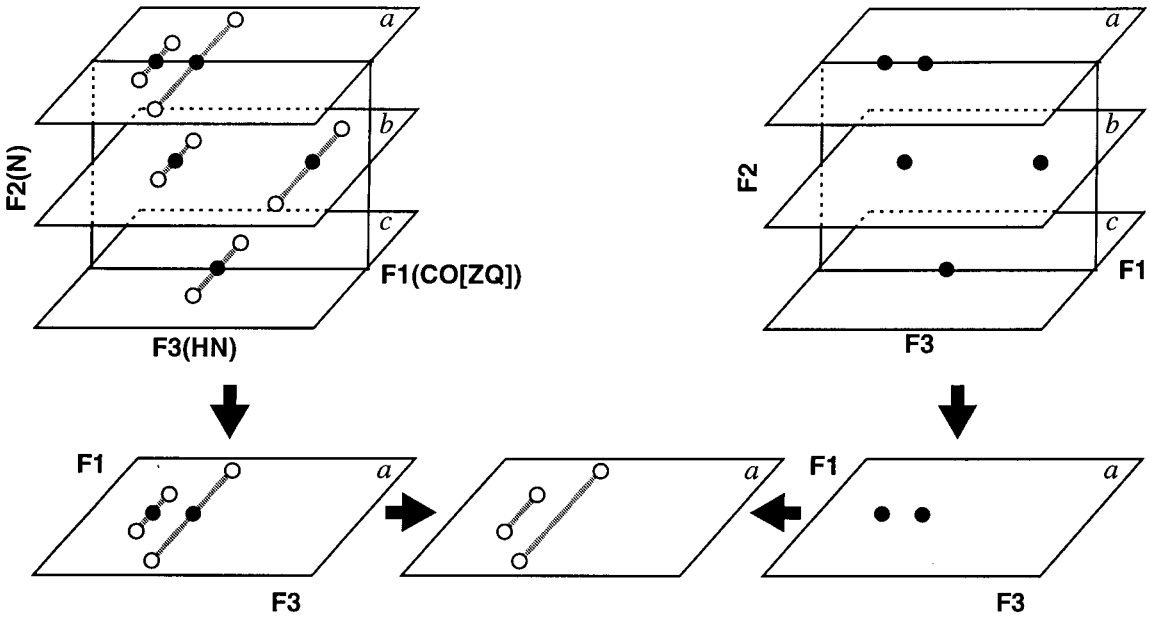


**Figure 10.** Schematic illustration of the subtraction procedure which eliminates axial peaks (filled circles) from a 3D data set containing zero-quantum correlations (open circles). (Note that the axial peaks are subtracted out automatically when double-quantum data sets are generated). A 3D data set containing only axial peaks is generated (right-hand side) by recording a 2D ($t_2$,$t_3$) data set and reconstructing a 3D ($t_1$,$t_2$,$t_3$) data matrix using software written in-house. Subsequently the two 3D time-domain data sets are subtracted and the resultant 3D data matrix processed as usual. Alternatively, the data sets can be subtracted in the frequency domain, as illustrated in the figure. By subtracting each $F_1-F_3$ plane in the "axial" data set (right-hand side) from the corresponding planes taken from the original ZQ data set (left-hand side) a new ZQ data set is obtained without axial correlations (center). This is illustrated for $F_1-F_3$ plane "a" in the figure.

**Acknowledgment.** This research has been supported by the Medical Research Council of Canada and the Natural Sciences and Engineering Research Council of Canada. Drs. Tanja Kortemme and Luis Serrano (EMBL) are thanked for providing the $^{15}N$,$^{13}C$,$^{2}H$-labeled sample used in this research. Drs. Vladimir Malkin and Olga Malkina (Slovak Academy of Sciences) are thanked for providing the latest version of deMon software. N.R.S. would like to acknowledge a postdoctoral fellowship from FCAR, Quebec. L.E.K. is a foreign investigator of the Howard Hughes Medical Research Institute.

**Supporting Information Available:** One figure illustrating the signal-to-noise ratio of correlations in DQ and ZQ spectra of the spectrin SH3 domain recorded at 600 MHz, one table of $R_{DQ} - R_{ZQ}$ rates for residues in the spectrin SH3 domain measured at 500 and 600 MHz, and one table of $^{13}CO$ CSA tensors obtained from DFT computations. This material is available free of charge via the Internet at http://pubs.acs.org.

## Appendix

As discussed in the Description of the Experiments section, $^{15}N$ transverse magnetization can evolve under either $^1J_{NC\alpha}$, $^1J_{NCO}$ or $^2J_{NC\alpha}$, $^1J_{NCO}$ couplings during the $2T_N$ periods in the scheme of Figure 1a. Evolution resulting from $^1J_{NC\alpha}$, $^1J_{NCO}$ couplings gives rise to the double- and zero-quantum correlations of interest in spectra. In contrast, evolution from $^2J_{NC\alpha}$, $^1J_{NCO}$ couplings results in axial peaks in the $F_1$ dimension since a term of the form $C^{\alpha}_z(i-1)N_z(i)$ is created at point **b** in the scheme of Figure 1a which does not evolve during $t_1$. It is possible to suppress these axial peaks by a time-domain deconvolution procedure.[30] In cases where double- and zero-quantum peaks are close to the carrier in the $^{13}CO$ dimension ($\pm$0.4 ppm), however, this can distort the intensities of these peaks. We prefer, therefore, to employ an alternative approach, based on subtracting an additional 3D data set containing only axial peaks from the full data matrix. One approach might be to record a second 3D matrix with the $^{13}CO$ 90° pulse of phase y (at the end of the constant-time $t_1$ period) removed. This pulse has no effect on the axial peaks; however, its removal ensures that double- and zero-quantum signals of interest are not refocused into observable magnetization by the end of the sequence. Hence subtraction of this "axial" 3D from the full data set eliminates the axial peaks and enables quantification of DQ and ZQ correlations that are close to zero frequency in $F_1$. There is, however, a more time-effective approach, outlined in Figure 10. The key is to realize that the axial peaks derive from signal that does not evolve during $t_1$; that is, the ($t_1$,$t_2$,$t_3$) data set containing only axial peaks is simply a set of identical ($t_2$,$t_3$) planes. It is possible, therefore, to generate such a 3D matrix simply by recording a 2D ($t_2$,$t_3$) data set and reconstructing a 3D time-domain profile. Subsequently this 3D data set can be subtracted from the original 3D data set (containing DQ and ZQ correlations in addition to axial peaks). In fact, it is only necessary to subtract the reconstructed 3D time-domain data from the zero-quantum time-domain data. This is because separate double- and zero-quantum time-domain data are typically obtained by subtracting/adding data sets recorded in an interleaved manner as described above. In this way, axial peaks are suppressed directly in the double-quantum data set. Note that care must be taken to ensure that the axial peaks are of the same intensity in the "axial" and original 3D data sets. Suppose that the 2D and 3D data sets are acquired with k and m scans, respectively. Because the zero-quantum time domain data set is generated from interleaved data (each with m scans) the "axial" 3D must be multiplied by 2m/k prior to subtraction from the original time-domain data.

JA0000201